Title: Variant-to-gene mapping identifies *ARHGEF12* as a primary open-angle glaucoma effector gene

Authors: Vrathasha Vrathasha[1,8,†], Matthew C. Pahl[2,3,†], Jie He[1,8], Mina Halimitabrizi[1,8], Moksha Laxmi[1,8], Rebecca Salowe[1], Struan F. A. Grant[2,3,4,5,6,7,9,†], Joan M. O'Brien[1,8,*†]

†Authors contributed equally
* Corresponding author: Penn Medicine Center for Genetics of Complex Disease, 25 N 38th St, Philadelphia, PA 19104 (joan.obrien@pennmedicine.upenn.edu; phone: 215-900-4204)

Affiliations:

1. Center for Genetics of Complex Disease, Scheie Eye Institute, Department of Ophthalmology, University of Pennsylvania, Philadelphia, PA 19104, USA
2. Center for Spatial and Functional Genomics, The Children's Hospital of Philadelphia, Philadelphia, PA 19104, USA.
3. Division of Human Genetics, The Children's Hospital of Philadelphia, Philadelphia, PA 19104, USA
4. Department of Genetics, Perelman School of Medicine, University of Pennsylvania, Philadelphia, PA 19104, USA.
5. Department of Pediatrics, University of Pittsburgh School of Medicine, Pittsburgh, PA 19104, USA
6. Department of Pediatrics, Perelman School of Medicine, University of Pennsylvania, Philadelphia, PA 19104, USA.
7. Division of Diabetes and Endocrinology, The Children's Hospital of Philadelphia, 3615 Civic Center Boulevard, Philadelphia, PA 19104, USA
8. F.M. Kirby Center for Molecular Ophthalmology, University of Pennsylvania, Philadelphia, PA 19104, USA
9. Department of Genetics, Perelman School of Medicine, University of Pennsylvania, Philadelphia, PA, USA

Abstract: Primary open-angle glaucoma (POAG) is the most prevalent subtype of glaucoma. It has a strong inherited component and disproportionately affects individuals of African ancestry. To date, trans-ethnic meta-analyses of genome-wide association studies (GWAS) have revealed 329 unique risk loci for POAG and related traits. Such studies have annotated the gene nearest to a given GWAS signal as an effector gene, but this assumption has proven frequently incorrect. Indeed, the actual effector gene can be located tens or hundreds of kilobases distal to the GWAS signal, influencing disease pathogenesis via long-range interactions. The Primary Open-Angle African Ancestry Glaucoma Genetics (POAAGG) study previously conducted a mega-analysis across 11,275 subjects of African ancestry, revealing 46 POAG risk loci. To implicate putative causal variants and their corresponding effector genes that they may functionally impact, we assayed for gene expression, chromatin accessibility, and chromatin conformation, using RNA-seq, ATAC-seq, and Hi-C, respectively, in human trabecular meshwork cells (hTMCs) and retinal ganglion cells derived from human induced pluripotent stem cells (hiPSC-RGCs). Our analyses implicated 24 genes in hTMCs and 56 genes in hiPSC-RGCs. We further prioritized implicated variants based on concordant findings in other POAG genetic studies and their reported roles in eye physiology. Using quantitative real-time PCR (qRT-PCR), we assessed differences in the expression of genes targeted by the select risk variants in hTMCs and hiPSC-RGCs derived from control and POAG subjects. Among the suggested genes, *ARHGEF12* was selected for further validation as it was previously implicated by our GWAS data; it was studied using hiPSC-RGCs from donors homozygous for either the risk or non-risk allele. We observed that the risk genotype exhibited decreased *ARHGEF12* expression, distinct morphological features, and altered neuronal activity as measured by calcium imaging. Integrating GWAS findings with chromatin maps enabled us to implicate POAG causal variants and their corresponding effector genes in two ocular cell types, providing researchers with novel risk variants and targets to investigate functionality in a comparable fashion to follow-up of *ARHGEF12*.

Introduction:

Over the past two decades, genome-wide association studies (GWAS) have revealed thousands of single-nucleotide polymorphisms (SNPs) that are statistically associated with complex phenotypes and disease risk. The vast majority of these GWAS-implicated signals are located in non-coding regions of the genome, presumably influencing disease susceptibility by altering the expression of one or more target genes [1-3]. However, the assumption that the nearest gene to the GWAS-implicated signal represents the true effector gene has proven insufficient, as a non-coding element does not automatically regulate its nearest gene [3,4]. Effector genes can be located tens or hundreds of kilobases distal to regulatory elements due to long-range interactions at the 3D genome level [1,5-9]. Promoters, enhancers, and boundary elements interact in dynamic higher-order chromatin structures within the 6.5 gigabases of DNA in the human genome, leading to contacts between different regions [10,11]. Thus, given this complexity, the interpretation of GWAS signals has been limited to date, as GWAS itself does not unambiguously reveal which target genes correspond to the discovered signals, hindering the interpretation of potential disease mechanisms [6].

Historically, the study of 3D genome organization has been challenging due to a lack of relevant methodologies. However, over the past decade, many innovative approaches to map genome architecture have emerged, deepening our understanding of the structural organization of the genome and the regulatory mechanisms of genes. Chromosome conformation capture (3C)-based techniques and novel methods of 3D genome organization analysis, such as Hi-C and its derivatives, allow the mapping of putative contacts across a variety of genomic distances [12,13]. These approaches can connect putative causal variants as genetic association signals to the actual culprit effector gene, allowing diagnostic and therapeutic approaches to be explored with greater confidence when the true target is actually being pursued.

Structural genomics approaches have been successfully applied to several complex genetic disorders, implicating novel risk genes. For example, over 100 risk loci have been associated with breast cancer, with many mapping to non-protein-coding regions and “gene deserts.” Hi-C chromatin maps identified 110 putative target genes mapping to 33 loci, producing a shortlist of candidates for follow-up studies [14]. For type 2 diabetes, 3D genomic approaches also revealed that an intronic SNP in the *TCF7L2* gene, widely considered one of the strongest loci for this disease[15], is not the sole causal gene at this locus, but rather also functions as a regulatory region for *ACSL5* [16]. Similar approaches in osteoporosis [3], obesity [17-19], carpal tunnel syndrome [6], type 2 diabetes [20], and rheumatoid arthritis [21] have similarly implicated novel causal target genes that drove functional follow-up studies.

However, such 3D genomic efforts in the context of primary open-angle glaucoma (POAG) remain limited, despite the disorder being a leading cause of irreversible blindness worldwide [22-24]. POAG has a strong heritability component, ranging from 13% to 81% [25-28]. Several monogenic mutations have been reported for POAG, but they account for only 5% of all cases [29-32]. Thus, the majority of POAG genetic risk is considered attributable to polygenic architecture. Thus far, GWAS analyses have identified 329 POAG loci, as well as multiple risk loci associated with endophenotypes such as cup-to-disc ratio (CDR), intraocular pressure (IOP), central corneal thickness

(CCT), and retinal nerve fiber layer (RNFL) thinning [33-49]. However, the vast majority of these loci are harbored in non-coding areas of the genome and therefore do not directly pinpoint the underlying specific gene(s), cell types, or mechanisms [35]. Translating these results to biological insights requires systematic identification of putative causal variants and the corresponding candidate effector genes, together with functional verification in either cellular or animal models [20,50,51]. Applying a 3D genomics approach to POAG will provide researchers with both novel and confirmed targets for functional investigation. Indeed, Wang *et al* already reported that using scATAC-seq-derived peaks in the human retina could assign a SNP (rs4821699), located in the intronic region of *TRIOBP,* as a contributing causal variant to glaucoma by altering the gene's expression in retinal ganglion cells (RGCs) [4].

In this study, we employed 3D-genomic approaches to implicate causal variants and their corresponding effector genes at POAG loci uncovered in a large population of African ancestry individuals. We generated 3D genomics data using two glaucoma-related ocular cell lines: human trabecular meshwork cells (hTMCs) and RGCs derived from human induced pluripotent stem cells (hiPSC-RGCs), as it is known that gene regulatory elements are cell-type and tissue-specific.

Our analyses implicated 24 genes in hTMCs and 56 genes in hiPSC-RGCs, including *ARHGEF12*. As this gene was prioritized by multiple signals in both cell types, it was previously implicated by fine-mapping analyses in our prior GWAS [33], and has an established role in IOP regulation [37]. From this triangulation of evidence, *ARHGEF12* was selected for subsequent analysis as its function in RGCs remains poorly understood. Using qRT-PCR, we detected significant differences in the mRNA expression of *ARHGEF12* in hTMCs and hiPSC-RGCs derived from POAG and control subjects. We also observed marked differences in mitochondrial structure and a significant decrease in the intensity of spike firing rate of hiPSC-RGCs carrying the *ARHGEF12* variant compared to the control hiPSC-RGCs.

Results:

Construction of chromatin contact maps for hiPSC-RGCs and hTMCs

In order to implicate candidate causal variant-effector gene pairs for POAG-associated loci, we identified putative cis-regulatory elements (cREs) harboring proxy SNPs using ATAC-seq and chromatin contacts using promoter-focused Capture C to implicate the corresponding target effector genes in hTMCs and HiC in hiPSC-RGCs. Additionally, we generated RNA-seq of both models to contextualize the gene expression in these cells (**Figure 1a**).

For hiPSC-RGCs, we sequenced an average of 697.8 million reads for ATAC-seq, 197 million reads for RNA-seq, and 2.94 billion reads for Hi-C per replicate. Similarly, for hTMCs, we generated 169 million reads for ATAC-seq, 125.4 million reads for RNA-seq, and 995.8 million reads for Promoter-focused Capture C for hTMCs (**Figure S1a**). Libraries passed other QC metrics such as the expected fragment size distribution and proportion of long-range cis-reads in the chromatin interaction data (**Figure S1c,e**).

First, we focused on identifying open chromatin regions (OCRs) that may act as regulatory elements to influence gene expression. Using standard approaches to call significant ATAC-seq peaks ($q < 0.05$), we identified 132,634 OCRs in hTMCs and 255,543 OCRs in hiPSC-RGCs that were reproducible in at least two replicates in each cell type. We observed that approximately 26% of these OCRs were shared between both cell types (**Figure 1b**).

As expected, the majority of OCRs were located in non-coding regions such as introns and intergenic regions **(Figure 1c)**. We then mapped these OCRs to effector genes using matched chromatin conformation data. We considered both proximal OCRs overlapping promoter regions themselves and those overlapping distal promoter-interacting regions defined by Hi-C or Promoter-focused Capture C, as well as distal OCRs **(Figure 1d)**. The significant distal promoter interaction regions were considered using either Chicago [52] for Promoter-focused Capture C data (Chicago Score > 5), and the combination of Mustache [53] and FitHiC2 [54] was used as performed previously to call interaction in the hiPSC-RGC HiC data[3,20]. We intersected the resulting loop calls with ATAC-seq peaks to define a set of promoter-interacting region OCRs (PIR-OCRs), which may function as long-distance cis-regulatory elements to influence gene expression. We further considered the set of OCRs located locally to a promoter (-1500/+500bp of the TSS) to be promoter OCRs.

A comparable number of promoter contacts was detected between the hiPSC-RGCs and hTMCs, with HiC also identifying a greater number, as it does not enrich specific contacts (**Figure 1e**). A subset of these were interactions involving one or more promoters (promoter-to-promoter interactions; p2p). Comparing the distance between these interactions, we detected that non-promoter to promoter interactions called by hiPSC-RGC HiC were longer than those called by Capture C in hTMCs. However, the same difference was not observed for promoter-to-promoter interactions across cell types **(Figure 1f)**. Overall, our approach identified 34,709 OCRs in interactions with 17,977 distinct genes in hTMCs and 39,496 OCRs contacting 19,174 genes in hiPSC-RGCs.

Promoters interacting with open chromatin regions are associated with gene expression

Next, we validated the association of promoter contacts across OCRs in the context of gene regulation. We first identified the number of OCRs called per gene, which was a mean of 5.0 in hTMCs and 6.2 in hiPSC-RGCs (**Figure 2a**). Similarly, we examined the mean number of genes connected per OCR, which was 2.6 in hTMCs and 2.5 in hiPSC-RGCs (**Figure 2b**). Given that multiple genes may be implicated at a GWAS locus, we next sought to characterize the promoter-promoter and promoter-regulatory elements. We found 9.2% of genes in hiPSC-RGCs and 12.1% of genes in hTMCs were in promoter–promoter interactions with at least one other distinct gene. The number of connected OCRs per gene was positively correlated with gene expression across both cell types (**Figure 2c**), suggesting that these interactions capture functional regulatory elements.

Next, we sought to examine whether the number of OCRs contacting promoters correlated with differences in genes between the two cell types. We identified differentially expressed genes between hiPSC-RGC and hTMCs. Given that we expected big differences in expression between these two cellular models, we employed stringent criteria, as our primary goal in this analysis was to identify cellular marker genes. The significance threshold was considered with |logFC| > 5; FDR < 1×10^{-6} for genes to be considered as differentially expressed. We observed 2831 genes enriched in hTMCs and 12,316 genes enriched in hiPSC-RGCs (**Figure S2a; Table S1**), which may reflect greater cellular diversity in generated hiPSC-RGCs. Reassuringly, known hTMCs and retinal neuron genes were detected, as the gene with the highest enrichment in hTMCs cells was Fibronectin 1, which is related to flow through the TMCs (*FN1*) [55], and in hiPSC-RGCs was Cerebellar Degeneration Related 1 (*CDR1*), which is involved in retinal neuron survival [56]. Likewise, pathway enrichment analysis revealed enrichment of cytoskeletal, adhesion, and stress response pathways in hTMCs, as well as rhodopsin signaling (FDR = 0.08) in hiPSC-RGCs (**Figure S2b**). When we correlated the difference in the number of OCR contacts with gene expression, we observed a moderate correlation (Spearman's Rho = 0.159, P < 2.2e-19; **Figure 2d**). This correlation may be limited because chromatin accessibility does not distinguish between active enhancers and other mechanisms that regulate gene expression. Taken together, these results are consistent with the expectation that increased chromatin contacts are positively associated with gene expression and may contribute to differences in expression across cell types.

Heritability enrichment for eye-relevant traits in regulatory elements

Next, to determine which traits were enriched in our datasets, we conducted partitioned LD score regression to assess enrichment of polygenic signals within genomic annotations across several eye-related traits. We included recent GWAS studies for vision-relevant traits, such as myopia and age-related macular degeneration, from publicly available summary statistics of GWAS in European populations (**Figure 3; Table S2**). We detected significant enrichments for myopia (hTMC: Enrichment= 9.9, FDR= 7.1×10^{-6}; hiPSC-RGC: Enrichment= 3.9, FDR= 5.9×10^{-3}) [57], primary outer angle glaucoma (hTMC: Enrichment= 10.9, FDR= 1.9×10^{-3}; hiPSC-RGC: Enrichment= 3.8, FDR= 0.07) [36], intraocular pressure (hTMC: Enrichment= 17.9, FDR= 1.3×10^{-3}; hiPSC-

RGC: Enrichment= 7.03, FDR= 0.03) [58], progressive vision loss (hTMC: Enrichment= 5.39, FDR= 0.02; hiPSC-RGC: Enrichment= 3.1, FDR= 0.049) [59], and Macular Telangiectasia (hTMC: Enrichment= 18.9, FDR= 0.086; hiPSC-RGC: Enrichment = 15.7, FDR = 0.049) [60]. For most traits that were enriched in both cell types, the hTMCs displayed stronger enrichment compared to hiPSC-RGCs, except for Macular Telangiectasia, a retinal disease [60]. We did not detect significant enrichment in retinoschisis [57]. Taken together, these analyses suggest that our datasets can serve as a useful resource for investigating the non-coding contribution of eye-relevant traits.

While LD score regression is useful for adjusting for genetic confounding and heritability enrichment, the complexity of long-distance LD has limited its application for recently admixed groups, such as African Americans. Recently, LD score regression has been extended to accommodate these issues in covariate-adjusted LDSC [61], which extends the LD window and uses principal components from the LD matrix as covariates for the regression. To this end, we performed partitioned LD score regression using our annotations with our recent African ancestry-based GWAS [33]. While the GWAS sample size is slightly under the signal, we detected nominal significance with strong enrichment only in hTMCs (hTMC: Enrichment= 17.2, Unadjusted *P*=0.044). This result, combined with the significant result in the European POAG study, motivated us to pursue variant-to-gene mapping for genome-wide significant POAG variants [33].

Variant-to-gene mapping of genome-wide significant African ancestry GWAS loci for POAG

Taking 46 sentinel variants representing independent signals that reached genome-wide significance [33], we first expanded to proxy variants in strong linkage disequilibrium (LD; $r^2 > 0.6$) using either the sample matrix or TOPMED-LD [62] and LDLink 1000G reference databases [63]. This query yielded a total of 4,432 proxy variants, with ~56% agreement between two or more approaches (**Figure S3a**). We then intersected these variants with OCRs that displayed significant chromatin contacts to a gene promoter, identifying 44 variants in hiPSC-RGCs that were collectively in contact with 56 genes (**Table S3**). Among the loci investigated, our approach nominated at least one gene for 20 loci (42.6%).

From this list of putative effector genes, we prioritized variants based on: (1) overlap of findings from our prior orthogonal approaches, such as GWAS, and implication in other genetic studies of POAG (such as the *ARHGEF12* variant), (2) genes involved in neuronal function (*UCHL1, TUBB2B* and its associated lincRNA *LINC02525*), (3) genes involved in other retinal degeneration diseases (*CRB1* and *EXOSC2*), (4) antioxidant (*CAT*), (5) molecules involved in key cellular pathways of eye development such as Rho/Rho-associated kinase (ROCK) and Notch signaling pathways (*ARHGEF12*, *ROCK1*, *MIB2*, *MTA1* and its associated lincRNA *AL928654.1*).

We analyzed the mRNA expression of the selected variants in hTMCs isolated from human donor control eyes and POAG patients who underwent trabeculectomy. First, we validated the authenticity of the isolated hTMCs by performing myocilin induction experiments using qRT-PCR. We determined that dexamethasone-treated hTMCs expressed significantly higher *myocilin* levels relative to untreated hTMCs (**Figure S4a-e**), which confirmed that the isolated primary cells were indeed TMCs [57]. When comparing mRNA expression of variants in hTMCs isolated from control and POAG

subjects, we found that *ARHGEF12* and *ROCK1* were significantly elevated (4 ± 0.13, p = 0.0001) and (2.75 ± 0.12, p = 0.0001), respectively, in hTMCs obtained from a POAG patient carrying a heterogeneous SNP (rs11824032G>A). Similarly, *MIB2* was significantly elevated (1.72 ± 0.12, p = 0.0007) in POAG hTMCs with a homogeneous SNP (rs4320726). However, there was no significant difference in the expression of *CAT* (**Figure 4a-d**). Genotype information for the variants associated with the tested genes in each hTMC line is listed in **Table S6**.

Analysis of mRNA expression of variants in hiPSC-RGCs generated from control and POAG line carrying the *ARHGEF12* variant showed that *ARHGEF12* was significantly downregulated (0.35 ± 0.5, p = 0.006) in the POAG hiPSC-RGCs. Similarly, *TUBB2B* (0.05 ± 0.07, p < 0.0001), *LINC02525* (0.015 ± 0.1, p < 0.0001), *EXOSC2* (0.048 ± 0.07, p < 0.0001), *UCHL1* (0.57 ± 0.15, p = 0.03), and *CRB1* (0.53 ± 0.15, p = 0.01) genes were all significantly downregulated in POAG hiPSC-RGCs compared to control cells. However, there was no significant difference in the expression of *ROCK1* and *MTA1*/ *AL928654.1* (**Figure 4e-m**). Genotype information for each of the genes in the hiPSC-RGC lines is listed in **Table S7.**

Functional validation of *ARHGEF12* variant in patient-derived hiPSC-RGCs

We identified *ARHGEF12* through fine mapping and colocalization analyses [33]. We detected two variants (rs34002948 and rs11824032) corresponding to two independent signals (r^2 = 0) with contacts to promoters of this locus in hiPSC-RGCs (**Figure 5a**). We predicted transcription factor motifs likely to be either strengthened or disrupted by these variants (**Figure 5b**). rs11824032 was predicted to disrupt several Kruppel-like zinc finger family motifs, while rs34002948 was predicted to strengthen affinity for several nuclear receptor family members. Among these, *NR1I3* and *KLF1* were the strongest expressed in hiPSC-RGCs (**Figure 5c**). The variant rs11824032 was located in close proximity to the transcription start site (TSS) (<5kb), whereas the other was implicated through a long-distance interaction (~1 Mb) spanning several genes. Indeed, this gene was moderately expressed (TPM =1.57) in control hiPSC-RGCs, which cumulatively led us to prioritize the *ARHGEF12* gene for functional validation.

We re-contacted subjects from our POAAGG study and, using Sanger sequencing, confirmed that they had a homozygous SNP (rs11824032G>A) at the *ARHGEF12* gene (**Figure S5b**) and we utilized a matched control with the wild-type *ARHGEF12* gene (**Figure S5a**). We collected blood, isolated peripheral blood mononuclear cells (PBMCs), and reprogrammed these into hiPSCs, which were later differentiated into RGCs in culture following our previously described protocol [58-60]. The 2D hiPSC-RGC differentiation developed in our laboratory yields a large population of pure RGCs in an accelerated and less labor-intensive manner, without the use of gene modification techniques. On day 35, fluorescence-activated cell sorting (FACS) analysis of hiPSC-RGCs carrying the *ARHGEF12* variant expressed the following RGC-specific markers: BRN3 (87%) and SNCG (92%) (**Figure S5d**). Similarly, hiPSC-RGCs from the control subject carrying the wild-type *ARHGEF12* gene expressed BRN3 (96%) and SNCG (92%) markers (**Figure S5c**).

Using western blot, we observed a trend toward decreased levels of ARHGEF12 protein (0.79 ± 0.24) in hiPSC-RGCs derived from the POAG line (n = 3), but this difference was not statistically significant (**Figure 5d-e**). However, ultrastructural

analyses by transmission electron microscopy (TEM) revealed marked morphological differences between control and disease variant hiPSC-RGCs. Control cells exhibited elongated mitochondria with intact cristae and dense, well-organized cytoplasm consistent with normal metabolic activity, whereas *ARHGEF12* variant cells displayed swollen, vacuolated mitochondria, cytoplasmic disorganization, and accumulation of autophagic vacuoles containing undigested material (**Figure 5f**). These results highlight variant-linked cellular vulnerability.

To investigate the functional effects of the *ARHGEF12* variant on RGC function, fluorescent Ca^{2+} indicators were used to indirectly measure the neuronal activity of hiPSC-RGCs [61-63]. Light-evoked intracellular calcium responses by hiPSC-RGCs treated with BioTracker™ 609 Red Ca^{2+} AM dye were imaged using a laser scanning confocal microscope. Changes in fluorescence intensity linearly corresponded with spike rates in control and disease variant hiPSC-RGCs, respectively (**Videos 5a and 5b**). We analyzed the fluorescence responses of over 200 spontaneously firing RGCs from each hiPSC line subjected to 559 nm laser stimulation and detected a variety of response dynamics. However, averaged across all cells, significant changes in fluorescence intensity were noted between the two hiPSC-RGC lines (**Figure 5g**). Total activities of the RGCs in control and *ARHGEF12* variant expressing hiPSCs, expressed as the sum of all RGC amplitudes, were 53 ± 1.75% (n = 215) and 28 ± 0.82% (n = 213), respectively (**Figure 5h**).

Discussion:

POAG is a type of optic neuropathy characterized by progressive loss of RGCs and degeneration of the optic nerve. RGCs are the only projection neurons in the retina, responsible for collecting all visual information processed by other retinal neurons and transmitting it through the optic nerve to visual targets in the brain. The contributing factors in the pathogenesis of POAG are not fully understood; however, it is known that increased resistance to the aqueous humor outflow pathway by trabecular meshwork cells leads to elevated intraocular pressure, which causes the death of RGCs [64].

Glaucoma is a highly heritable disease, but the genes identified thus far account for less than 10% of all cases [65]. The mechanisms underlying this disease, which is the leading cause of irreversible blindness in the world today, remain very poorly understood. As a result of this unmet medical need, more than 30% of affected individuals do not respond to any currently available therapy [66,67]. GWAS has uncovered a large number of POAG loci, but they represent a challenge to translate, given that the vast majority reside in non-coding regions of the genome and confer relatively small effect sizes. Here, we sought to identify SNP-to-target gene relationships and elucidate the roles of non-coding variants in POAG progression and pathogenesis. We integrated variants implicated by our large GWAS in the most affected and understudied African ancestry individuals with gene expression analysis, accessible chromatin peaks, and 3D chromatin architecture maps in two glaucoma-specific cell types, namely hiPSC-RGCs and hTMCs.

We employed ATAC-seq to map OCRs in direct contact with regulatory elements of a target gene, influencing its expression [68-70]. We also utilized Hi-C, which reveals the spatial organization of chromatin within a nucleus and identifies long-range chromosomal interactions between promoter-promoter, promoter-enhancer, or promoter-gene [71-73]. Together, these two techniques generated a list of putative variants in POAG-associated cell types. Our analysis implicated 24 genes in hTMCs and 56 genes in hiPSC-RGCs. Furthermore, RNA-seq analysis was conducted to investigate the impact of these variants on gene expression in each of the cell types. These cell-type-specific lists of variants will aid in our understanding of the gene-regulatory networks leading to vision loss in POAG patients.

One of the genes of interest implicated in hiPSC-RGCs was the *ARHGEF12* gene. This gene has been associated with POAG by several orthogonal approaches. Previous GWAS reports revealed an association between the *ARHGEF12* locus and vertical CDR and IOP at the following lead variants: rs58073046 [37,47], rs199800298 [36], rs2305013 [37], and 11:120357425 [74]. Furthermore, our group identified genetic co-localization between the lead variant (rs11824032) mapping to *ARHGEF12* and baseline CDR [33]. Therefore, we selected *ARHGEF12* for further characterization in hiPSC-RGCs based on a cumulation of evidence indicating its association with POAG [37,75].

EyeBrowse, an eye-centric genome browser, has shown that *ARHGEF12* is expressed in the trabecular meshwork, retina, and optic nerve [76]. Furthermore, *Arhgef12* transcripts were detected in RGCs at P14 in mice [77]. It is widely reported that ARHGEF12 binds directly to ABCA1 and RhoA/RhoA kinase proteins; the signaling pathway is known to reduce trabecular meshwork plasticity, thereby increasing resistance to aqueous humour outflow and subsequently increasing IOP [78-80]. However, there is very limited knowledge of its functional role in the retina or RGCs. In our study, mRNA

analysis of the *ARHGEF12* transcripts in hTMCs was significantly elevated, whereas in hiPSC-RGCs, the mRNA expression was significantly downregulated in the POAG line. Using western blot, we observed that the POAG hiPSC-RGCs produced lower levels of ARHGEF12 protein compared to control hiPSC-RGCs.

Additionally, we assessed the RGC pathophysiology of control and POAG hiPSC-RGCs with the *ARHGEF12* variant by evaluating its functional activity using advanced imaging techniques and visual stimuli. Neuronal activity of hiPSC-RGCs was measured using Ca^{2+}, which can be optically monitored, as synaptic responses and action potential firing typically evoke rapid changes in intracellular free calcium. Thus, the dynamic changes in intracellular Ca^{2+} levels within hiPSC-RGCs are coupled to the electrical properties of this neuron, thus indirectly reflecting its activity. Ca^{2+} imaging within hiPSC-RGCs revealed dramatic changes in light-evoked activities between control and glaucomatous conditions. We detected significant differences in fluorescence changes between control and disease variant hiPSC-RGCs, which were 53 ± 1.75% (n = 215) and 28 ± 0.82% (n = 213), respectively. In comparison, the reported $\Delta F/F0$ of naive RGCs in a wild-type mouse retina is ~150-200% [81]. Single-cell patch clamp recordings were conducted on control and variant carrying hiPSC-RGCs, yielding inconclusive results (data not shown) [82-85]. Given that only a few hiPSC-RGCs fired spontaneously, it appears that single-cell patch clamp recording, which tests individual cells one at a time, may not be an efficient methodology for investigating the effects of a variant on overall RGC function.

Since ARHGEF12 is part of the Rho/ROCK signaling pathway, we investigated its downstream mediators. The Rho/ROCK pathway is involved in the synthesis of the extracellular matrix in the aqueous humour, leading to contraction of TMCs and increased resistance to the outflow pathway that subsequently increases IOP within the eye [86-93]. Therefore, the molecules involved in this pathway have been the target of many anti-glaucoma treatments [94,95]. ROCK inhibitors have been shown to provide optic nerve neuroprotection, to improve survival of RGCs, and to promote axonal regeneration [96-98]. In this study, we detected a significant overexpression of *ROCK1* transcripts in POAG hTMCs carrying a heterogeneous SNP (rs11824032G>A) at the *ARHGEF12* gene. But, there was no significant difference in the *ROCK1* expression between control and POAG hiPSC-RGCs.

Here, we have elaborated on our reasoning for choosing genes implicated in hTMCs from our study for additional analysis, such as *CAT* and *MIB2*. TMCs are highly sensitive to oxidative damage; in fact, several studies have reported that the progression of POAG may be due to reduced antioxidant capacity of the TMCs [99-101]. Therefore, the presence of the *CAT* variant, an antioxidant, in our list warranted further investigation. Serum samples collected from patients with POAG have been reported to exhibit low levels of catalase (CAT) [102]. However, in our study, we did not detect a significant difference in *CAT* expression between control and POAG hTMCs. Another gene of interest from our hTMC list was the *MIB2* gene, which encodes the E3 ubiquitin protein ligase involved in Notch signaling, a pathway crucial for eye development. Furthermore, the Mouse Genome Informatics database has reported that a mouse model of *Mib2* deficiency exhibits variable neural tube closure defects and abnormal eye morphology [103,104]. We detected a significant difference in *MIB2* expression between control and POAG hTMCs with a homogeneous SNP (rs4320726).

Similarly, we investigated the mRNA expressions of several genes of interest from our putative list in hiPSC-RGCs, such as *TUBB2B/ LINC02525*, *CRB1*, *EXOSC2*, *UCHL1*, and *MTA1*/ *AL928654.1*. For example, the *TUBB2B* gene (*LINC02525*, its associated lincRNA) encodes for ß-tubulin, which is a crucial building block for cell structure in neurons. Mutations in this gene have been reported to affect neuronal migration and axonal guidance, resulting in severe malformations [105,106]. In our study, *TUBB2B* and *LINC02525* mRNA expressions were significantly downregulated in POAG hiPSC-RGCs carrying the *ARHGEF12* SNP. Another group reported a similar finding, where NMDA-mediated exotoxicity downregulated *ARHGEF12* and *TUBB2B* expression in neurons [107]. Similarly, the *UCHL1* gene encodes for a ubiquitin enzyme. This gene is specifically expressed in neurons and is involved in the maintenance of synaptic function [108,109] and its expression was significantly downregulated in POAG hiPSC-RGCs. Whereas *CRB1* [110-114] and *EXOSC2* [115] are genes with known roles in other retinal degeneration diseases, such as retinitis pigmentosa and Leber congenital amaurosis, and their expression was also significantly downregulated. *Arhgef12* is reported to be a modifier gene variant that contributes to *CRB1*-associated retinal dystrophy in mice [116]. In the case of *MTA1*/ *AL928654.1*, we detected contacts between rs187398392, an accessible proxy, and the Metastasis-associated protein (*MTA1)* gene and associated lncRNA (*AL928654.1*/*MTA1-DT*), which are both established cancer genes. While *MTA1* has not been implicated in POAG, it has a known role in retinal development through interactions with SIX3, which regulates the number of retinal cells during development [117]. In this study, we did not detect significant difference in the expression of *MTA1* and *AL928654.1* between control and POAG hiPSC-RGCs.

Since this study was designed specifically to research the significance of the most relevant variant rs11824032 associated with *ARHGEF12*, we only identified POAAGG subjects with and without the risk allele to generate hiPSCs. Hence, we did not control for the other variants. Therefore, we are currently combining our hiPSC-RGC system with CRISPR/Cas9, as it enables the assessment of the effects of a specific mutation in characterizing RGC dysfunction and retinal degeneration. Using CRISPR/Cas9-mediated prime editing, we will install and/or correct specific POAG-associated edits in hiPSCs, generating isogenically paired cell lines with a single genetic background with minimal variability, to overcome a significant obstacle when using patient-derived hiPSCs to evaluate genotype-to-disease phenotype relationships. Thus far, the efficiency of our CRISPR/Cas9-prime editing of the *ARHGEF12* SNP (rs11824032G>A) in HEK293T cells is ~15-20% (**Figure S6**), and we will build on this for installation in hiPSCs.

In conclusion, we sought to identify SNP-to-target gene relationships and to elucidate how coding and non-coding variants contribute to POAG pathogenesis. We matched a subset of linkage disequilibrium-expanded variant lists to those in OCRs (peaks from ATAC-seq) that contact a gene promoter (significant chromatin contacts called from Hi-C). Our analysis implicated 24 genes in hTMCs and 56 genes in hiPSC-RGCs. Of these genes, *ARHGEF12* was previously implicated in our GWAS study. Using qRT-PCR, we confirmed a significant difference in the expression of *ARHGEF12* in hTMCs and hiPSC-RGCs derived from POAG case and control subjects. Furthermore, we detected significant differences in light-evoked responses between control and the POAG hiPSC-RGCs carrying the *ARHGEF12* variant. This extensive variant-to-gene dataset will serve as a key resource to the POAG community going forward.

Limitations: The present hiPSC-RGC analysis of the *ARHGEF12* variant should be considered preliminary, as our study did not delve into understanding how the variant affects RGC function or which RGC subtypes are most significantly impacted. Similarly, the Ca^{2+} results for the disease variant should be interpreted with caution, as light stimulation of hiPSC-RGCs with high intensity and long duration may generate artifacts. Furthermore, we only measured the intracellular calcium signal and not the actual electrical signal produced by the RGCs.

Additionally, POAG is a complex polygenic disease; instead of studying one variant at a time to assess its pathogenicity, we can use pooled CRISPR screens to package a bulk of CRISPR gRNA-containing plasmids and transduce them into hiPSCs [118]. The stable expression of gRNAs facilitates the overexpression or knockout of targeted genes. The hiPSCs can then be differentiated into RGCs in culture, and the integrated gRNAs can be sequenced via next-generation sequencing (NGS). Enriched or depleted gRNAs in the RGCs may provide information about the potential involvement of the corresponding gene(s) in RGC function and POAG pathogenesis.

Materials and Methods:

Human iPSC culture

Undifferentiated hiPSCs were generated and characterized at the University of Pennsylvania iPSC Core Facility, providing a comprehensive analysis of hiPSC characteristics [119-121]. The University of Pennsylvania and the Children's Hospital of Philadelphia Human Subjects Research Institutional Review Boards approved all human sample collection protocols consistent with the Declaration of Helsinki. All methods were performed in accordance with the relevant research guidelines and regulations of the University of Pennsylvania. Written informed consent was obtained from all human cell donors. The hiPSCs were maintained in StemMACs iPSC-Brew XF (Miltenyi Biotec, catalog #: 130-107-086, North Rhine-Westphalia, Germany) containing 50X supplement (Miltenyi Biotec, catalog #: 130-107-087, North Rhine-Westphalia, Germany), and Pen Strep (Life Technologies, catalog #: 10378-016, Carlsbad, CA, USA). Demographics of the patients from whom the hiPSCs were generated are listed in **Table S4**.

Retinal progenitor cell (RPC) generation and conditions

hiPSCs were cultured on Matrigel-coated plates (Corning, catalog #: 354230, Corning, NY, USA) in 37°C, 5% O_2, and 5% CO_2 conditions. Cells were maintained until they reached 75% confluency. hiPSCs were then split and seeded in one well of a 6-well tissue culture dish (Corning, catalog #: 229106, Corning, NY, USA) coated with 1:100 diluted Matrigel growth factor. hiPSCs were maintained at 37 °C, 5% O_2, and 5% CO_2 until reaching 100% confluence then transferred to 37 °C, 5% CO_2 overnight prior to induction. On day 0, iPSC-Brew media was changed to RPC induction media: DMEM/F12 (50:50; Corning, catalog #: 10-092-cm, Corning, NY, USA), 1% Pen Strep (Life Technologies, catalog #: 10378-016, Carlsbad, CA, USA), 1% Glutamine MAX (Life Technologies, catalog #: 35050-061, Carlsbad, CA, USA), 1% NEAA (Life Technologies, catalog #: 11140-050, Carlsbad, CA, USA), 0.1 mM 2-ME (Life Technologies, catalog #: 21985-023, Carlsbad, CA, USA), 2% B27 supplement (w/o vitamin A; Life Technologies, catalog #:

12587-010, Carlsbad, CA, USA), 1% N2 supplement (Life Technologies, catalog #: 17502-048, Carlsbad, CA, USA), containing 2 μM XAV939 (X) (Wnt inhibitor; R&D Systems, catalog #: 3748, Minneapolis, MN, USA), 10 μM SB431542 (SB) (TGF-β inhibitor; R&D Systems, catalog #: 1614, Minneapolis, MN, USA), 100 nM LDN193189 (L) (BMP inhibitor; R&D Systems, catalog #: 6053, Minneapolis, MN, USA), 10 mM nicotinamide (Sigma-Aldrich, catalog #: N0636, St. Louis, MO, USA), and 10 ng/mL IGF1 (R&D Systems, catalog #: 291-G1, Minneapolis, MN, USA). Cultures were fed daily for 4 days. On day 4, the culture medium was exchanged for RPC induction media containing 2 μM XAV939, 10 μM SB431542, 100 nM LDN193189, 10 ng/mL IGF-1, and 10 ng/mL bFGF. The media was changed daily for 21 days [54].

Retinal ganglion cell (RGC) differentiation

Before RGC differentiation, the medium was changed daily using iNS media containing 250 ng/mL Shh (R&D Systems, catalog #: 8908-SH, Minneapolis, MN, USA), 100 ng/mL FGF8 (R&D Systems, catalog #: 423-F8, Minneapolis, MN, USA) for 2 days. For RGC differentiation on day 24, cells were manually crossed into small clusters with Leibovitz's medium containing 34 μM D-Glucose (Research Products International, catalog #: G32045-500, Mt. Prospect, IL, USA) using the crosshatching technique as previously described [122], then re-plated at a density of 1.0×10^5 cells/well of 6-well plate coated with 1:100 diluted Matrigel growth factor in RGCs induction media containing: 100 ng/mL Follistatin 300 (R&D Systems, catalog #: 669-FO, Minneapolis, MN, USA), 0.5 μM Cyclopamine (R&D Systems, catalog #: 1623/1, Minneapolis, MN, USA), 3 μM DAPT (Stemgent, catalog #: 04-0041, Cambridge, MA, USA), and 4.2 μM Y-27632 dihydrochloride (Rock inhibitor; R&D Systems, catalog #: 1254/1, Minneapolis, MN, USA). The media was changed 24 hours post-plating with RGC induction media containing 100 ng/mL Follistatin 300 and 3 μM DAPT daily for 2 days. From day 27, media was changed to RGC induction media containing: 3 μM DAPT, 10 μM Rock inhibitor (Y27632), 5 μM Forskolin (Selleckchem, catalog #: S2449, Houston, TX, USA), 400 μM N^6,2′-O-Dibutyryladenosine 3′,5′- cyclic monophosphate sodium salt (cAMP; Sigma-Aldrich, catalog #: D0627, St. Louis, MO, USA), 40 ng/mL BDNF (R&D Systems, catalog #: 248-BDB, Minneapolis, MN, USA), 5 ng/mL NT4 (R&D systems, catalog #: 268-N4, Minneapolis, MN, USA), and 10 ng/mL CNTF (R&D systems, catalog #: 257-NT, Minneapolis, MN, USA). The media was changed every 2-3 days until day 36. After maturation (D36), the medium was exchanged every 3-4 days with RGC induction media containing 3 μM DAPT and 10 μM Rock inhibitor (Y27632) [54].

Human trabecular meshwork (TM) cells

For the 3D genomic experiments, such as RNA-seq, ATAC-seq and Hi-C, Primary trabecular meshwork cells were used, which were commercially obtained (ScienCell, catalog #: 6590, Carlsbad, CA, USA).

For the functional validation of the variants, hTM tissue strips were isolated either from whole globes or obtained from glaucoma patients during trabeculectomy surgery at the Scheie Eye Institute. hTM tissues isolated from post-mortem donor eyes were obtained from the National Disease Research Interchange (NDRI). Whole globes were bisected near the equator, and the iris, lens, and ciliary processes were gently removed from the anterior segment. The anterior segment was then divided into two half-wedges.

Using fine-tipped forceps, hTM tissue was grasped at the cut edge of each wedge and gently pulled away. Each hTM strip was cut into three pieces. hTM tissue from whole globes and trabeculectomy (typically 0.5–1 mm) was incubated for 30 minutes in DMEM (Gibco, catalog #: 11885-084, Waltham, MA, USA) containing 10 mg/mL dispase (Gibco, catalog #: 17105-041, Waltham, MA, USA) and 10 mg/mL collagenase (Gibco, catalog #: 17104-019, Waltham, MA, USA) at 37°C. Tissues were washed once with DMEM, then placed onto gelatin-coated plates with coverslips. hTM pieces from whole globes were distributed into three wells of a 6-well plate, while surgical hTM tissue was placed in one well. Coverslips were positioned to secure the tissue, and DMEM supplemented with 10–20% FBS (Cytiva Hyclone, catalog #: SH30910.03, Logan, UT, USA) and penicillin-streptomycin (Gibco, catalog #: 15140-122, Waltham, MA, USA) was applied. Culture media was replaced every five days. Once the hTMCs reached confluence. Cultures were expanded further as needed or cryopreserved for long-term storage [53].

We validated the authenticity of the hTMCs by performing MYOC induction experiments with 100 nM dexamethasone (Sigma-Aldrich, catalog #: D4902, St. Louis, MO, USA), freshly added to the media every 2–3 days for two weeks, which significantly increased *MYOC* expression by qRT-PCR relative to untreated controls [53]. For all our experiments, we used primary TM cultures from Passage 2 (P2) to Passage 4 (P4). Demographics of the patients from whom the hTMCs were isolated are listed in **Table S5**.

Sanger sequencing

DNA was extracted from hTMCs, control, and *ARHGEF12* disease-variant hiPSC-RGCs using the Purelink genomic DNA mini kit (Invitrogen, catalog #: K1820-01, Waltham, MA, USA). DNA was quantified using the Qubit dsDNA BR assay kit (Invitrogen, catalog #: Q32853, Waltham, MA, USA) and Qubit 2.0 fluorometer. PCR was performed using the GoTag Green master mix (Promega, catalog #: M7122, Madison, WI, USA), and the primer sets are listed in **Table S9**. PCR products were purified using Gel and PCR cleanup kit (Macherey-Nagel, catalog #: 74069.250, Düren, Germany) and submitted for Sanger sequencing at the Penn Genomic and Sequencing Core. Sequencing data were analyzed using NCBI BLAST and the UGENE (Unipro) software.

hiPSC-Retinal Neuron and Trabecular Meshwork Cell ATAC-seq

A total of 50,000 to 100,000 cells were centrifuged at 500 xg for 5 min at 4°C. The cell pellet was washed with cold PBS and resuspended in 50 µL of cold lysis buffer (10 mM Tris-HCl, pH 7.4, 10 mM NaCl, 3 mM MgCl2, 0.1% NP-40/IGEPAL CA630) and immediately centrifuged at 550 xg for 10 min at 4°C. Nuclei were resuspended in the Nextera transposition reaction mix (25 µL 2x TD Buffer, 2.5 µL Nextera Tn5 transposase (Illumina, USA Cat #FC-121-1030), and 22.5 µL nuclease-free H2O) on ice, then incubated for 45 min at 37°C. The tagmented DNA was then purified using the Qiagen MinElute kit, eluted with 10.5 µL Elution Buffer (EB). Ten microliters of purified tagmented DNA were PCR amplified using Nextera primers for 12 cycles to generate each library. The PCR reaction was subsequently cleaned up using 1.5x AMPureXP beads (Agencourt, Beverly, MA, USA), and concentrations were measured by Qubit. Libraries were paired-end sequenced using an Illumina NovaSeq 6000 (CHOP 51 bp read length).

Image files were demultiplexed using bcf2fastq (v, Illumina, San Diego, CA, USA). Fastq files were aligned to hg38 using Briefly, pair-end reads from three biological replicates for each cell type were aligned to hg38 genome using bowtie2, and duplicate reads were removed from the alignment. Narrow peaks were called independently for each replicate using macs2 (-p 0.01 --nomodel --shift -75 --extsize 150 -B --SPMR --keep-dup all -callsummits), and ENCODE blacklist regions were removed from peaks in individual replicates. The reproducible peak set (ATAC-seq peaks called by MACS peaks called with q-value < 0.01) was used as the consensus OCRs for each cell type. ATAC-seq fragment distribution plots were generated using the fragSizeDist function from the Bioconductor package ATACseqQC (v 1.28.0) with the deduplicated bam files.

hiPS-RGC HiC

For the hiPS-RGC, Hi-C libraries were prepared for three biological replicates using the Arima-HiC kit (Arima Genomics, catalog #: A410030, Carlsbad, CA, USA), according to the manufacturer's protocols. Briefly, cells were crosslinked using formaldehyde. Crosslinked cells were then subject to the Arima-HiC protocol, which utilizes multiple restriction enzymes (targeting ^GATC and G^ANTC) to digest chromatin. Arima-HiC sequencing libraries were prepared by first shearing purified proximally ligated DNA and then size-selecting 200–600 bp DNA fragments using AmpureXP beads (Beckman Coulter, catalog #: A63882, Brea, California, USA). The size-selected fragments were then enriched using Enrichment Beads (provided in the Arima-HiC kit) and then converted into Illumina-compatible sequencing libraries with the Swift Accel-NGS 2S Plus DNA Library Kit (Swift, catalog #: 21024, Ann Arbor, MI, USA) and Swift 2S Indexing Kit (Swift, catalog #: 26148, Ann Arbor, MI, USA). The purified, PCR-amplified DNA underwent standard QC (qPCR, Bioanalyzer, and KAPA Library Quantification (Roche, catalog #: KK4824, Basel, Switzerland)) and was sequenced with unique single indexes on the Illumina NovaSeq 6000 Sequencing System at 2x51 base pairs. For one of these biological replicates, two technical replicates were performed to fill the appropriate S4 flow cell.

Trabecular Meshwork Promoter Capture C

For the hTM library, 107 fixed cells were thawed at 37ºC, followed by centrifugation at RT for 5 mins at 1845 xg. The cell pellet was resuspended in 1 mL of dH2O supplemented with 5 µL 200X protease inhibitor cocktail, incubated on ice for 10 minutes, and then centrifuged. Cell pellet was resuspended to a total volume of 650 µL in dH2O. 50 µL of cell suspension was set aside for pre-digestion QC, and the remaining sample was divided into 3 tubes. Both pre-digestion controls and samples underwent a pre-digestion incubation in a Thermomixer (BenchMark, Tempe, AZ, USA) with the addition of 0.3% SDS, 1x NEB DpnII restriction buffer, and dH2O for 1 hour at 37ºC, shaking at 1,000 rpm. A 1.7% solution of Triton X-100 was added to each tube, and shaking was continued for another hour. After pre-digestion incubation, 10 µL of DpnII (NEB, 50 U/µL) was added to each sample tube only and continued shaking along with pre-digestion control until the end of the day. An additional 10 µL of DpnII was added to each digestion reaction, and the mixture was digested overnight. The next day, an additional 10 µL of DpnII was added, and the mixture continued to shake for another 2-3 hours. 100 uL of each digestion reaction was then removed, pooled into one 1.5 mL tube, and set aside for digestion

efficiency QC. The remaining samples were heat-inactivated by incubating at 1000 rpm in a MultiTherm for 20 minutes at 65°C to inactivate the DpnII, followed by cooling on ice for an additional 20 minutes. Digested samples were ligated with 8 uL of T4 DNA ligase (HC ThermoFisher, 30 U/µL) and 1X ligase buffer at 1,000 rpm overnight at 16°C in a MultiTherm.

The next day, an additional 2 µL of T4 DNA ligase was spiked into each sample and incubated for another few hours. The ligated samples were then de-crosslinked overnight at 65°C with Proteinase K (20 mg/mL; Denville Scientific, Holliston, MA, USA) along with pre-digestion and digestion control. The following morning, both controls and ligated samples were incubated for 30 min at 37°C with RNase A (Millipore, Burlington, MA, USA), followed by phenol/chloroform extraction, ethanol precipitation at -20°C, the 3C libraries were centrifuged at 1000 xg for 45 min at 4°C to pellet the samples. The controls were centrifuged at 1845 xg. The pellets were resuspended in 70% ethanol and centrifuged as described above. The pellets of 3C libraries and controls were resuspended in 300 µL and 20 µL dH2O, respectively, and stored at −20°C. Sample concentrations were measured by Qubit. Digestion and ligation efficiencies were assessed by gel electrophoresis on a 0.9% agarose gel and by quantitative PCR (SYBR green; Thermo Fisher, Waltham, MA, USA).

Isolated DNA from 3C libraries was quantified using a Qubit fluorometer (Life Technologies, Carlsbad, CA, USA), and 10 µg of each library was sheared in dH2O using a QSonica Q800R to an average fragment size of 350bp. The QSonica settings used were 60% amplitude, 30 seconds on, 30 seconds off, with 2-minute intervals, for a total of 5 intervals at 4 °C. After shearing, DNA was purified using AMPureXP beads (Agencourt, Beverly, MA, USA). DNA size was assessed using a Bioanalyzer 2100 with a DNA 1000 Chip (Agilent, Santa Clara, CA, USA), and DNA concentration was determined via Qubit. SureSelect XT library prep kits (Agilent, Santa Clara, CA, USA) were used to repair DNA ends and for adaptor ligation following the manufacturer's protocol. Excess adaptors were removed using AMPureXP beads. Size and concentration were verified using a Bioanalyzer with a DNA 1000 Chip and a Qubit fluorometer before hybridization. One microgram of adaptor-ligated library was used as input for the SureSelect XT capture kit using the manufacturer's protocol and our custom-designed 41K promoter Capture-C library. The quantity and quality of the captured library were assessed using a Bioanalyzer with a high-sensitivity DNA Chip and a Qubit fluorometer. SureSelect XT libraries were then paired-end sequenced on the Illumina NovaSeq 6000 platform (CHOP; 51 bp read length).

HiC and Promoter Capture C data were processed using the HiCUP pipeline (v0.7.4). Significant chromatin contacts were called with Chicago (Score > 5) [52] for Promoter-focused Capture C data (Chicago Score > 5), and used the combination of Mustache (FDR < 0.1) [53] and FitHiC2 (FDR < 1x10-6) [54] as performed previously [3,20].

RNA-seq

RNA was isolated from ~1 million of each cell type using Trizol Reagent (Invitrogen, Waltham, MA, USA), purified using the Directzol RNA Miniprep Kit (Zymo Research, Irvine, CA, USA), and depleted of contaminating genomic DNA using DNAse I. Purified RNA was checked for quality on a Bioanalyzer 2100 using the Nano RNA Chip, and

samples with RIN > 7 were used for RNA-seq library preparation. RNA samples were depleted of rRNA using QIAseq Fastselect RNA removal kit (Qiagen, Hilden, Germany). Samples were then processed for library preparation using the SMARTer Stranded Total RNA Sample Prep Kit (Takara Bio, Kusatsu, Shiga, Japan) according to the manufacturer's instructions. Briefly, the purified first-strand cDNA is amplified into RNA-seq libraries using SeqAmp DNA Polymerase and the Forward and Reverse PCR Primers from the Illumina Indexing Primer Set HT for Illumina. The quality and quantity of the libraries were assessed using the Agilent 2100 Bioanalyzer system and Qubit fluorometer (Life Technologies, Carlsbad, California, USA). Sequencing of the finalized libraries was performed on the NovaSeq 6000 platform at the CHOP Center for Spatial and Functional Genomics.

RNA-seq was processed using the STAR (v 2.7.9a) pipeline, aligned to hg38 with gencode V30 as the reference. Reads were counted using HTSeq (v2.0.2), and TPM values were calculated using the effective gene length.

Differential expression analysis was conducted using standard procedures in the edgeR framework [128]. First gene counts were aggregated across technical replicates. Low-expressed genes were then filtered using the filterByExpr function with the default parameters. Normalization was performed with the trimmed-median of the means method implemented in calcNormFactors. Dispersions were estimated with replicate cell types as a group and parameter robust = TRUE. The model of 0 ~ cell type was fitted using glmQLFit with parameter robust = TRUE and tested with glmQFLTest across the cell type contrast. P-values were adjusted using the Benjamini-Hochberg procedure. Given the extreme differences observed between cell types, we opted for a strict cutoff of abs(logFC) > 7 and FDR < 1e-6 to focus on the strongest differential marker genes. TPM values were calculated as previously described using the effect-gene length [129]. Pathway enrichment was conducted using the hypergeometric test implemented in phyper in R (R Core Team, 2021).

LD score regression:

We checked our chromatin annotations for GWAS heritability enrichment using LD-score regression implemented in LDSC [130]. Publicly available EUR summary statistics were processed using the munge_sumstats.py script provided with ldsc (https://github.com/bulik/ldsc). Annotation files were constructed using open chromatin regions defined for hTMCs or hiPSC-RGCs. For European GWAS studies, LD score regression (v 1.01) [130,131] was run using the European 1000 Genomes Phase3 reference data and developer-provided baseline v2.2 reference files [132]. Enrichment analyses were run with the default parameters, with the exception of –print-coefficients set. Tests were adjusted with Bonferroni correction and false discovery rate (FDR) using the R function p-adjust. Dot plots were generated using the ggplot2 package (v. 4.0.1). For AFR ancestry analyses, covariate-adjusted LD score regression [133] was used to adjust enrichment estimates for recent admix ancestry by incorporating principal components calculated and using an expanded LD window. To construct the reference, the hg38 1000G plink reference files were retrieved from the plink website. Principal components were computed using the eigenstrat smartpca function [134] with the default parameters except numoutevac: 10. These were used in conjunction with the bed file for the 52 binary baseline annotations, as well as hTMC and hiPSC-RGCs as above, to build

annotations with --ld-wind-cm set to 20 as previously described [133]. This was used as the annotation to calculate enrichment as above.

Genomic Analyses

Comparative analyses for promoter contacts: TPM values were correlated with the number of promoter-connected OCRs using the Spearman correlation coefficient, implemented in the cor.test function with method="speaman" from R (v4.4.0).

SNP selection and LD expansion: Sentinel SNPs were collected from our previous African American GWAS [33]. These were expanded to any SNPs in high LD ($R^2 > 0.6$) with the signal from the LD matrix of the population, or the EUR/AFR variants from the 1000 genomes high coverage set from LDLink [135] or TOPMED-LD [136].

Variant to gene mapping: Using the expanded set of genome-wide significant GWAS sentinels and their proxy variants, we then intersect variants with the set of OCRs that either overlapped known promoter regions (−1500/+ 500 bp of gencode V30 TSS) or OCR overlapping promoter interacting regions identified by Capture C/HiC in either hiPSC-RGCs or hTMCs. Genomic coordinate overlaps were identified using the R package GenomicRanges (ver 1.56.2) against the hg38 genome reference.

Transcription factor motif disruption: We used motifbreakR (v.2.19.5) [137] to predict transcription factors that may have disrupted binding by the highlighted variants (rs11824032, rs34002948, rs187398392). Position weight matrices from hocomoco v10 [138] were queried against the hg38 genome with the reference and alternative allele. Motifs with strong disruption were predicted using the motifBreakR function, with parameters: filterp = TRUE, threshold = 1e-3, method = "ic", bkg = c(A=0.25, C=0.25, G=0.25, T=0.25), and BPPARAM=BiocParallel::bpparam(). P-values were calculated with the calculatePvalue() function. The TPM-adjusted expression values were then plotted to identify which of the putative regulators may act in hiPSC-RGCs.

FACS analysis

hiPSC-RGC cultures were lifted using TrypLE Express (Invitrogen, catalog #: 12605-010, Waltham, MA, USA) and collected by centrifugation at 1600 rpm for 5 minutes at 4 °C. The pelleted cells were resuspended in 1X PBS supplemented with 0.5% bovine serum albumin and 0.1% sodium azide (FACS buffer). Cells were fixed in 4% paraformaldehyde (v/v) for 15 min at room temperature (RT), followed by permeabilization using 0.5% Tween-20 (v/v) for 10 min at RT. Cells were incubated with anti-BRN3 Alexa Fluor 594 (Santa Cruz, catalog #: sc-390780, Santa Cruz, CA, USA) and anti-SNCG Alexa Fluor 488 (Santa Cruz, catalog #: sc-65979, Santa Cruz, CA, USA). Stained cells were analyzed using LSRFortessa B in the Penn Cytomics and Cell Sorting Shared Resource Laboratory at the University of Pennsylvania (RRID:SCR_022376). The data were further analyzed using FACS software (FlowJo 10.8.1, Ashland, OR, USA).

qRT-PCR

Total RNA was extracted from hTMCs and hiPSC-RGCs using RNeasy® Mini Kit (Qiagen, catalog #: 74104, Hilden, Germany). For each sample, 150 ng of total RNA was reverse transcribed using the SuperScript® III first-strand cDNA synthesis kit (Invitrogen, catalog #: 18080-051, Waltham, MA, USA). Amplified cDNA was quantified using Fast SYBR™ Green Master Mix (Applied Biosystems, catalog #: 4385612, Foster City, CA, USA) on a QuantStudio 6 Pro (Applied Biosystems, Foster City, CA, USA), and the primer sets are listed in **Table S8**. All results were normalized to a *GAPDH* housekeeping control and were from three technical replicates for each experimental condition. The relative gene expression was compared to that of control cells to obtain normalized gene expression, which is represented as the mean ± SEM.

Western blot

hiPSC-RGCs from control and *ARHGEF12*-variant lines were scraped off the dish and centrifuged at 1600 rpm for 5 minutes. The pellet was extracted using RIPA buffer (Cell Signaling, catalog #: 9806S, Danvers, MA, USA), which contained protease and phosphatase inhibitors (Roche, catalog #: 03115828001, Mannheim, Germany). Cells were sonicated (15 s X 3) and then incubated on ice for 20 minutes. After lysing the cells, cell debris was removed by centrifugation at 20,000 xg for 30 minutes, and the supernatant containing the cytoplasmic extract was transferred to a new tube. The protein content of the cell lysates was determined using the Qubit protein assay (Invitrogen, catalog #: Q33221, Waltham, MA, USA) with the Qubit 2.0 fluorometer and then normalized to ensure equal protein content. Protein extracts were analyzed using SDS-polyacrylamide gel electrophoresis with Mini-Protean precast gels (Bio-Rad, catalog #: 4561094, Hercules, CA, USA) and followed by a western blot. The samples were analyzed for ARHGEF12 protein (Life Technologies, catalog #: PA5143957, Carlsbad, CA, USA), and β-actin (Santa Cruz Biotechnology, catalog #: sc-47778, Santa Cruz, CA, USA) was used as the loading control. The experiments were repeated at least three times.

Transmission electron microscopy (TEM)

hiPSC-RGCs from a healthy control line and a POAG-associated *ARHGEF12*-variant line were cultured on 14-mm glass coverslips placed in a standard 24-well plate. Cells were plated at a density of 1×10^5 cells per well to achieve a uniform monolayer suitable for ultrastructural analysis. Cells were maintained under RGC differentiation conditions until they formed a healthy monolayer suitable for ultrastructural analysis.

Cells grown on coverslips were fixed with 0.1 M sodium cacodylate buffer (pH 7.4) containing 2.5% glutaraldehyde and 2.0% paraformaldehyde and incubated overnight at 4 °C. After thorough buffer washes, samples were post-fixed in 2.0% osmium tetroxide containing 1.5% potassium ferricyanide ($K_3Fe(CN)_6$) for 1 hour at room temperature, followed by rinsing with deionized water. En bloc staining was performed using 2% aqueous uranyl acetate.

The samples were then dehydrated through a graded ethanol series, infiltrated, and embedded in EMbed-812 resin (Electron Microscopy Sciences, Fort Washington, PA). Ultrathin sections were stained with uranyl acetate and Sato lead stain and examined

using a Talos L120C transmission electron microscope equipped with a Ceta 16 M digital camera.

Calcium imaging

Intracellular calcium within live hiPSC-RGCs was stained using BioTracker™ 609 Red Ca2+ AM Dye (Sigma-Aldrich, catalog #: SCT021, St. Louis, MO, USA). 8 µL of the dye (80 µM) was diluted in 902 µL of 1X PBS, along with 10 µL of Pluronic® F-127 (Sigma-Aldrich, catalog # 9003-11-6, St. Louis, MO, USA) and 80 µL of DMSO. hiPSC-RGCs were incubated with the diluted dye for 40 minutes at 37 °C. Images of cells were taken using a confocal laser scanning microscope. Images were acquired at a resolution of 256 x 256 pixels, at ~2 frames per second, and represented between 20 X 20 µm. Fluorescence responses in somas and dendrites were calculated with custom, ScanImage-compatible algorithms in Matlab. Fluorescent structures were outlined by hand using the roipoly function (Signal Processing Toolbox; The MathWorks). The fluorescence intensity of a neuron is reported throughout as the average intensity of all pixels over its soma, including the nucleus. Data was analyzed with custom software (Matlab; The MathWorks).

The mean time-dependent fluorescent signal from each RGC (*F*) was normalized by subtracting the mean pre-stimulus signal intensity *(F0)*, which is expressed as $\Delta F = F - F0$. The normalized neuronal responses ($\Delta F/F0$) for each RGC were then calculated [81,123].

Statistical analysis

For the quantitative gene and protein expression data, as well as ΔF/F0, all data are represented as mean ± SEM. Each experiment was conducted in triplicate for statistical analysis. Differences in gene transcript and protein expression, $\Delta F/F0$ between control and POAG hiPSC-RGCs and hTMCs were analyzed using the Student's *t* test for two-group comparison by statistical software (GraphPad Prism 6.0; GraphPad Software, Inc., La Jolla, CA, USA). *p-values of < 0.05 were considered statistically significant.

<u>Acknowledgements</u>

Funding/Support

This work was supported by the National Eye Institute, Bethesda, MD (1R01EY023557) and Vision Research Core (P30 EY001583) grants. Funds also came from the F.M. Kirby Foundation, Research to Prevent Blindness, UPenn Hospital Board of Women Visitors, and Paul and Evanina Bell Mackall Foundation Trust. The Ophthalmology Department at the Perelman School of Medicine and the VA Hospital in Philadelphia, PA, also provided support. The sponsors/funding organizations had no role in the design or conduct of this research. Penn Cytomics is partially supported by the Abramson Cancer Center NCI Grant (P30 016520). SFAG is supported by the Daniel B. Burke Endowed Chair for Diabetes Research.

Financial Disclosures

The authors have no financial disclosures.

Conflicts of Interest

The authors declare no conflicts of interest.

Authorship Contribution Statement

add if this is required for your journal at time of submission

Figure Legends

Figure 1: Constructing the cRE network of glaucoma-relevant cell types using ATAC-seq, RNA-seq, and chromatin conformation. (a) Schematic of the libraries constructed two cellular models of retinal neurons (hiPSC-RGCs) and trabecular meshwork cells (hTMCs). While RNA-seq and ATAC-seq were performed on both hiPSC-RGCs and hTMC, chromatin conformation was characterized via HiC in hiPSC-RGCs and Promoter Focused Capture C in hTMCs. (b) The number of open chromatin regions (OCRs) defined by ATAC-seq was found to be specific to each cell type (yellow = hTMCs; pink = hiPSC-RGCs). OCRs were considered shared if there was a 1bp overlap with an OCR in the opposite cell type. (c) The proportion of OCRs falling into each category of genomic region annotations (exons, introns, intergenic, or promoter). (d) Schematic of cases for overlaying chromatin conformation with open chromatin data. Regions with significant interactions in either Promoter Focused Capture C or HiC are termed Promoter Interacting Regions (PIR). OCRs overlapping such regions are considered putative cREs for the targeted promoter. OCRs that overlay promoters (-1500bp/+500bp from a TSS) themselves are also considered as potential regulatory elements. Variants located in OCRs and nominated by these approaches are considered potentially regulatory. (e) The number of contacts per cell type that are between a promoter and a non-promoter region, between two promoters, or between two non-promoter regions (only found in HiC). (f) The cumulative distribution of the distance of significant chromatin interactions called in hTMCs and hiPSC-RGCs, stratified by either promoter to non-promoter (p2c) or promoter to promoter (p2p).

Figure 2: Promoter-connected OCRs are correlated with increased expression. (a) The number of OCRs per gene vs the log-scaled number of genes with the specified number of OCRs in each cell type (pink = hiPSC-RGC; yellow = hTMC). (b) The number of genes connected per log-scaled OCR for each cell type. (c) The number of OCRs contacting a gene promoter vs expression quantified in log2(1+TPM) for each cell type. d) The difference in expression against the difference in the number of OCRs predicted to be connected to each gene. In (c) and (d), the trend line from the linear association is shown with the shaded region representing 95% confidence interval.

Figure 3: Dot plot depicting the results of partitioned LD score regression for hTMCs and hiPSC-RGCs across several European ancestry GWAS studies. Dot size depicts the size of enrichment and is colored by the coefficient z-score (higher corresponds to stronger association). * indicates the enrichment is significant following

Bonferroni correction, # indicates the result is significant following FDR correction, and ‡ indicates significance of the baseline-adjusted cell type coefficient FDR.

Figure 4: Quantitative mRNA expression analyses of prioritized genes implicated in hTMCs and hiPSC-RGCs. The quantitative expression profiles of the putative genes in hTMCs (a) *ARHGEF12,* (b) *ROCK1*, (c) *CAT*, and (d) *MIB2* and in hiPSC-RGCs (e) *ARHGEF12*, (f) *ROCK1*, (g) *TUBB2B*, (h) *LINC02525*, (i) *CRB1*, (j) *EXOSC2*, (k) *UHL1*, (l) *MTA1*, (m) *AL928654.1* using quantitative RT-PCR, with and without POAG.

Figure 5: Nomination of *ARHGEF12* as a putative effector gene for POAG AFR ancestry GWAS variant in hiPSC-RGCs. (a) Genomic track showing contact frequency, promoter contacts, and chromatin accessibility for *ARHGEF12.* Two implicated SNPs, rs11824032 and rs34002948, are highlighted. (b) Motifs predicted to be disrupted by these variants (circles = rs11824032; triangles = rs34002948). The x-axis is the difference in information content (log scale) relative to the alternative/reference alleles, with the -log10 P value on the y-axis. Color corresponds to the transcription factor name. (c) The expression level of predicted transcription factors and implicated genes across each replicate of hiPSC-RGC in the *ARHGEF12* locus. (d) Western blots depicting ARHGEF12 protein and (e) quantification of the levels in control and POAG hiPSC-RGCs. (f) Transmission electron microscopy (TEM) images revealing ultrastructural analyses of morphological differences between control and *ARHGEF12* variant hiPSC-RGCs. (g) Representative fluorescence response of firing control and POAG hiPSC-RGCs subjected to 559 nm laser stimulation. (h) The total sum of all RGC amplitudes in control and *ARHGEF12* variant expressing hiPSC-RGCs.

Figure S1: Quality control information for genome-wide assays. (a) Read counts for each biological replicate for ATAC-seq, either Promoter-focused Capture C (hTMCs) or HiC (hiPSC-RGC). (b) Fragment length distribution for ATAC-seq, depicting mononucleosome and dinucleosome peaks. (c) Valid 3C fragment class distribution (cis-close, cis-far, trans). Summary of promoter loop connections between promoters and OCRs for (d) hTMC and (e) hiPSC-RGCs.

Figure S2: Differential gene expression analysis between hTMCs and hiPSC-RGCs. (a) Volcano plot with the x-axis depicting the $\log_2$ fold change between hTMC (higher) and hiPSC-RGCs (lower). The y-axis depicts the -log10 transformed FDR value. (b) Dotplot depicts significantly enriched biological pathways from Camera analysis [140], the BioCarta collection on MSigDB [141], with dot size corresponding to -log10(FDR-adjusted P value), while color indicates cell type (pink = hiPSC-RGC; yellow = hTMC).

Figure S3: Summary of variant to gene mapping. To identify effector genes of African Ancestry POAG GWAS loci [33], we expanded sentinel variants by LD ($R^2 > 0.6$) using either the TOPMED-LD [136] or LDLink [135] reference databases. These variants were intersected with putative PIR-OCRs to identify the subset likely to be causal and their effector genes in hTMC and hiPSC-RGCs.

Figure S4: Characterization of the isolated hTM tissues by quantitative RT-PCR. We confirmed the presence of hTMCs isolated from human donor control eyes and POAG patients who underwent trabeculectomy using qRT-PCR. We determined that hTMCs

treated with 100 nM of dexamethasone expressed significantly higher *myocilin* levels relative to untreated hTMCs in (a) G01, (b) G03, (c) G06, (d) TM01, (e) TM07, and (f) TM036.

Figure S5: Characterization of the generated hiPSC-RGC lines. Sanger sequencing was performed to confirm the absence and presence of the rs11824032G>A variant in the *ARHGEF12* gene in (a) control hiPSCs and (b) POAG hiPSCs, respectively. FACS analysis was performed on the differentiated hiPSC-RGCs to confirm the presence of RGC-specific markers in (c) control hiPSC-RGCs and (d) POAG hiPSC-RGCs carrying the rs11824032G>A variant.

Figure S6: CRISPR/Cas9-editing of the *ARHGEF12* SNP in HEK293T cells. Bulk prime editing in HEK293T cells for installation of the *ARHGEF12* rs11824032 G/A SNV.

Supplementary Table Legends

Table S1: Differential gene expression analysis of hTMC and hiPSC-RGCs. logFC are relative to hTMC / hiPSC-RGC.

Table S2: Summary results for partitioned LDSR analyses conducted in hTMC and hiPSC-RGCs.

Table S3: Variant to gene mapping results for the latest African ancestry POAG GWAS study.

Table S4: Patient demographics of the generated hiPSCs.

Table S5: Patient demographics of the isolated hTMCs.

Table S6: Genotype information for the variants associated with the tested genes in each hTMC line.

Table S7: Genotype information for the variants associated with the tested genes in both hiPSC lines.

Table S8: Primer sequences for mRNA of selected putative genes.

Table S9: Primer sequences for genotyping selected variants using Sanger sequencing.

References

1. Maurano MT, Humbert R, Rynes E, et al. Systematic localization of common disease-associated variation in regulatory DNA. Science. 2012;337:1190–1195.

2. Gallagher MD, Chen-Plotkin AS. The Post-GWAS Era: From Association to Function. Am J Hum Genet. 2018;102:717–730.

3. Chesi A, Wagley Y, Johnson ME, et al. Genome-scale Capture C promoter interactions implicate effector genes at GWAS loci for bone mineral density. Nature Communications. 2019;10:1260.

4. Wang SK, Nair S, Li R, et al. Single-cell multiome of the human retina and deep learning nominate causal variants in complex eye diseases. Cell Genom. 2022;2:100164. doi: 10.1016/j.xgen.2022.100164. Epub 2022 Jul 27.

5. Schaub MA, Boyle AP, Kundaje A, et al. Linking disease associations with regulatory information in the human genome. Genome Res. 2012;22:1748–1759.

6. Pahl MC, Liu L, Pippin JA, et al. Variant to gene mapping for carpal tunnel syndrome risk loci implicates skeletal muscle regulatory elements. eBioMedicine. 2024;101:105038.

7. Ratnapriya R, Sosina OA, Starostik MR, et al. Retinal transcriptome and eQTL analyses identify genes associated with age-related macular degeneration. Nat Genet. 2019;51:606–610.

8. Marchal C, Singh N, Batz Z, et al. High-resolution genome topology of human retina uncovers super enhancer-promoter interactions at tissue-specific and multifactorial disease loci. Nature Communications. 2022;13:5827.

9. Orozco LD, Chen H, Cox C, et al. Integration of eQTL and a Single-Cell Atlas in the Human Eye Identifies Causal Genes for Age-Related Macular Degeneration. Cell Rep. 2020;30:1246–1259.e6.

10. Pombo A, Dillon N. Three-dimensional genome architecture: players and mechanisms. Nat Rev Mol Cell Biol. 2015;16:245–257.

11. Oudelaar AM, Higgs DR. The relationship between genome structure and function. Nature Reviews Genetics. 2021;22:154–168.

12. Jerkovic I, Cavalli G. Understanding 3D genome organization by multidisciplinary methods. Nat Rev Mol Cell Biol. 2021;22:511–528.

13. Bonev B, Cavalli G. Organization and function of the 3D genome. Nature Reviews Genetics. 2016;17:661–678.

14. Baxter JS, Leavy OC, Dryden NH, et al. Capture Hi-C identifies putative target genes at 33 breast cancer risk loci. Nat Commun. 2018;9:1028–9.

15. Palmer ND, Hester JM, An SS, et al. Resequencing and analysis of variation in the TCF7L2 gene in African Americans suggests that SNP rs7903146 is the causal diabetes susceptibility variant. Diabetes. 2011;60:662–668.

16. Xia Q, Chesi A, Manduchi E, et al. The type 2 diabetes presumed causal variant within TCF7L2 resides in an element that controls the expression of ACSL5. Diabetologia. 2016;59:2360–2368.

17. Smemo S, Tena JJ, Kim K, et al. Obesity-associated variants within FTO form long-range functional connections with IRX3. Nature. 2014;507:371–375.

18. Claussnitzer M, Dankel SN, Kim K, et al. FTO Obesity Variant Circuitry and Adipocyte Browning in Humans. N Engl J Med. 2015;373:895–907.

19. Rosen CJ, Ingelfinger JR. Unraveling the Function of FTO Variants. N Engl J Med. 2015;373:964–965.

20. Su C, Gao L, May CL, et al. 3D chromatin maps of the human pancreas reveal lineage-specific regulatory architecture of T2D risk. Cell Metab. 2022;34:1394–1409.e4.

21. Yang J, McGovern A, Martin P, et al. Analysis of chromatin organization and gene expression in T cells identifies functional genes for rheumatoid arthritis. Nature Communications. 2020;11:4402.

22. Quigley HA, Broman AT. The number of people with glaucoma worldwide in 2010 and 2020. Br J Ophthalmol. 2006;90:262–267.

23. Tielsch JM, Katz J, Sommer A, et al. Family history and risk of primary open angle glaucoma. The Baltimore Eye Survey. Arch Ophthalmol. 1994;112:69–73.

24. Muñoz B, West SK, Rubin GS, et al. Causes of blindness and visual impairment in a population of older Americans: The Salisbury Eye Evaluation Study. Arch Ophthalmol. 2000;118:819–825.

25. Cuellar-Partida G, Craig JE, Burdon KP, et al. Assessment of polygenic effects links primary open-angle glaucoma and age-related macular degeneration. Sci Rep. 2016;6:26885.

26. Teikari JM. Genetic factors in open-angle (simple and capsular) glaucoma. A population-based twin study. Acta Ophthalmol (Copenh). 1987;65:715–720.

27. Sanfilippo PG, Hewitt AW, Hammond CJ, et al. The heritability of ocular traits. Surv Ophthalmol. 2010;55:561–583.

28. van Koolwijk LME, Despriet DDG, van Duijn CM, et al. Genetic contributions to glaucoma: heritability of intraocular pressure, retinal nerve fiber layer thickness, and optic disc morphology. Invest Ophthalmol Vis Sci. 2007;48:3669–3676.

29. Awadalla MS, Fingert JH, Roos BE, et al. Copy number variations of TBK1 in Australian patients with primary open-angle glaucoma. Am J Ophthalmol. 2015;159:124–30.e1.

30. Rezaie R, Child C, Hitchings H, et al. Adult-Onset Primary Open-Angle Glaucoma Caused by Mutations in Optineurin. Science. 2002;295:1077–1079.

31. Stone EM, Fingert JH, Alward WL, et al. Identification of a gene that causes primary open angle glaucoma. Science. 1997;275:668–670.

32. Sakurada Y, Mabuchi F, Kashiwagi K. Genetics of primary open-angle glaucoma and its endophenotypes. Prog Brain Res. 2020;256:31–47.

33. Verma SS, Gudiseva HV, Chavali VRM, et al. A multi-cohort genome-wide association study in African ancestry individuals reveals risk loci for primary open-angle glaucoma. Cell. 2024;187:464–480.e10.

34. Singh N, Kizhatil K, Duraikannu D, et al. Structural framework to address variant-gene relationship in primary open-angle glaucoma. Vision Res. 2025;226:108505.

35. Choquet H, Wiggs JL, Khawaja AP. Clinical implications of recent advances in primary open-angle glaucoma genetics. Eye (Lond). 2020;34:29–39.

36. Choquet H, Paylakhi S, Kneeland SC, et al. A multiethnic genome-wide association study of primary open-angle glaucoma identifies novel risk loci. Nat Commun. 2018;9:2278–4.

37. Springelkamp H, Iglesias AI, Cuellar-Partida G, et al. ARHGEF12 influences the risk of glaucoma by increasing intraocular pressure. Hum Mol Genet. 2015;24:2689–2699.

38. Wiggs JL, Yaspan BL, Hauser MA, et al. Common variants at 9p21 and 8q22 are associated with increased susceptibility to optic nerve degeneration in glaucoma. PLoS Genet. 2012;8:e1002654.

39. Thorleifsson G, Walters GB, Hewitt AW, et al. Common variants near CAV1 and CAV2 are associated with primary open-angle glaucoma. Nat Genet. 2010;42:906–909.

40. Han X, Gharahkhani P, Hamel AR, et al. Large-scale multitrait genome-wide association analyses identify hundreds of glaucoma risk loci. Nat Genet. 2023;55:1116–1125.

41. Gharahkhani P, Jorgenson E, Hysi P, et al. Genome-wide meta-analysis identifies 127 open-angle glaucoma loci with consistent effect across ancestries. Nat Commun. 2021;12:1258–4.

42. Bailey JNC, Loomis SJ, Kang JH, et al. Genome-wide association analysis identifies TXNRD2, ATXN2 and FOXC1 as susceptibility loci for primary open-angle glaucoma. Nat Genet. 2016;48:189–194.

43. Gharahkhani P, Burdon KP, Fogarty R, et al. Common variants near ABCA1, AFAP1 and GMDS confer risk of primary open-angle glaucoma. Nat Genet. 2014;46:1120–1125.

44. Burdon KP. Genome-wide association studies in the hunt for genes causing primary open-angle glaucoma: a review. Clin Exp Ophthalmol. 2012;40:358–363.

45. Shiga Y, Akiyama M, Nishiguchi KM, et al. Genome-wide association study identifies seven novel susceptibility loci for primary open-angle glaucoma. Hum Mol Genet. 2018;27:1486–1496.

46. Lo Faro V, Bhattacharya A, Zhou W, et al. Novel ancestry-specific primary open-angle glaucoma loci and shared biology with vascular mechanisms and cell proliferation. Cell Rep Med. 2024;5:101430.

47. MacGregor S, Ong J, An J, et al. Genome-wide association study of intraocular pressure uncovers new pathways to glaucoma. Nat Genet. 2018;50:1067–1071.

48. Osman W, Low S, Takahashi A, et al. A genome-wide association study in the Japanese population confirms 9p21 and 14q23 as susceptibility loci for primary open angle glaucoma. Hum Mol Genet. 2012;21:2836–2842.

49. Chen Y, Lin Y, Vithana EN, et al. Common variants near ABCA1 and in PMM2 are associated with primary open-angle glaucoma. Nat Genet. 2014;46:1115–1119.

50. Galasko CS. Detection of bone metastases. Br Med J. 1977;1:1537–a.

51. Huang L, Rosen JD, Sun Q, et al. TOP-LD: A tool to explore linkage disequilibrium with TOPMed whole-genome sequence data. Am J Hum Genet. 2022;109:1175–1181.

52. Machiela MJ, Chanock SJ. LDlink: a web-based application for exploring population-specific haplotype structure and linking correlated alleles of possible functional variants. Bioinformatics. 2015;31:3555–3557.

53. Roayaei Ardakany A, Gezer HT, Lonardi S, et al. Mustache: multi-scale detection of chromatin loops from Hi-C and Micro-C maps using scale-space representation. Genome Biol. 2020;21:256–0.

54. Kaul A, Bhattacharyya S, Ay F. Identifying statistically significant chromatin contacts from Hi-C data with FitHiC2. Nat Protoc. 2020;15:991–1012.

55. Steely HT, Browder SL, Julian MB, et al. The effects of dexamethasone on fibronectin expression in cultured human trabecular meshwork cells. Invest Ophthalmol Vis Sci. 1992;33:2242–2250.

56. Schmelter C, Fomo KN, Brueck A, et al. Glaucoma-Associated CDR1 Peptide Promotes RGC Survival in Retinal Explants through Molecular Interaction with Acidic Leucine Rich Nuclear Phosphoprotein 32A (ANP32A). Biomolecules. 2023;13:1161. doi: 10.3390/biom13071161.

57. Keller KE, Bhattacharya SK, Borrás T, et al. Consensus recommendations for trabecular meshwork cell isolation, characterization and culture. Exp Eye Res. 2018;171:164–173.

58. Chavali VRM, Haider N, Rathi S, et al. Dual SMAD inhibition and Wnt inhibition enable efficient and reproducible differentiations of induced pluripotent stem cells into retinal ganglion cells. Scientific Reports. 2020;10:11828.

59. Gudiseva HV, Vrathasha V, He J, et al. Single Cell Sequencing of Induced Pluripotent Stem Cell Derived Retinal Ganglion Cells (iPSC-RGC) Reveals Distinct Molecular Signatures and RGC Subtypes. Genes. 2021;12.

60. Vrathasha V, Nikonov S, Bell BA, et al. Transplanted Human iPSC-derived Retinal Ganglion Cells Integrate into Mouse Retinas and are Electrophysiologically Functional. iScience. 2022:105308.

61. Tian L, Hires SA, Mao T, et al. Imaging neural activity in worms, flies and mice with improved GCaMP calcium indicators. Nat Methods. 2009;6:875–881.

62. Rumyantsev OI, Lecoq JA, Hernandez O, et al. Fundamental bounds on the fidelity of sensory cortical coding. Nature. 2020;580:100–105.

63. Chen Q, Cichon J, Wang W, et al. Imaging neural activity using Thy1-GCaMP transgenic mice. Neuron. 2012;76:297–308.

64. Weinreb RN, Aung T, Medeiros FA. The pathophysiology and treatment of glaucoma: a review. JAMA. 2014;311:1901–1911.

65. Kwon YH, Fingert JH, Kuehn MH, et al. Primary open-angle glaucoma. N Engl J Med. 2009;360:1113–1124.

66. Aptel F, Aryal-Charles N, Giraud J, et al. Progression of visual field in patients with primary open-angle glaucoma - ProgF study 1. Acta Ophthalmol. 2015;93:615.

67. Heijl A, Leske MC, Bengtsson B, et al. Reduction of intraocular pressure and glaucoma progression: results from the Early Manifest Glaucoma Trial. Arch Ophthalmol. 2002;120:1268–1279.

68. Dorgau B, Collin J, Rozanska A, et al. Single-cell analyses reveal transient retinal progenitor cells in the ciliary margin of developing human retina. Nat Commun. 2024;15:3567–x.

69. Buenrostro JD, Wu B, Chang HY, et al. ATAC-seq: A Method for Assaying Chromatin Accessibility Genome-Wide. Curr Protoc Mol Biol. 2015;109:21.29.1–21.29.9.

70. Pita-Thomas W, Gonçalves TM, Kumar A, et al. Genome-wide chromatin accessibility analyses provide a map for enhancing optic nerve regeneration. Scientific Reports. 2021;11:14924.

71. Lieberman-Aiden E, van Berkum NL, Williams L, et al. Comprehensive mapping of long-range interactions reveals folding principles of the human genome. Science. 2009;326:289–293.

72. Rao SSP, Huntley MH, Durand NC, et al. A 3D map of the human genome at kilobase resolution reveals principles of chromatin looping. Cell. 2014;159:1665–1680.

73. Lafontaine DLJ, Riback JA, Bascetin R, et al. The nucleolus as a multiphase liquid condensate. Nat Rev Mol Cell Biol. 2021;22:165–182.

74. Gao XR, Huang H, Nannini DR, et al. Genome-wide association analyses identify new loci influencing intraocular pressure. Hum Mol Genet. 2018;27:2205–2213.

75. Springelkamp H, Iglesias AI, Mishra A, et al. New insights into the genetics of primary open-angle glaucoma based on meta-analyses of intraocular pressure and optic disc characteristics. Hum Mol Genet. 2017;26:438–453.

76. Wistow G, Peterson K, Gao J, et al. NEIBank: genomics and bioinformatics resources for vision research. Mol Vis. 2008;14:1327–1337.

77. Macosko EZ, Basu A, Satija R, et al. Highly Parallel Genome-wide Expression Profiling of Individual Cells Using Nanoliter Droplets. Cell. 2015;161:1202–1214.

78. Wang J, Liu X, Zhong Y. Rho/Rho-associated kinase pathway in glaucoma (Review). Int J Oncol. 2013;43:1357–1367.

79. Fukuhara S, Chikumi H, Gutkind JS. Leukemia-associated Rho guanine nucleotide exchange factor (LARG) links heterotrimeric G proteins of the G(12) family to Rho. FEBS Lett. 2000;485:183–188.

80. Pattabiraman PP, Maddala R, Rao PV. Regulation of plasticity and fibrogenic activity of trabecular meshwork cells by Rho GTPase signaling. J Cell Physiol. 2014;229:927–942.

81. Li L, Feng X, Fang F, et al. Longitudinal in vivo Ca2+ imaging reveals dynamic activity changes of diseased retinal ganglion cells at the single-cell level. Proceedings of the National Academy of Sciences. 2022;119:e2206829119.

82. Wienbar S, Schwartz GW. The dynamic receptive fields of retinal ganglion cells. Prog Retin Eye Res. 2018;67:102–117.

83. Sanes JR, Masland RH. The types of retinal ganglion cells: current status and implications for neuronal classification. Annu Rev Neurosci. 2015;38:221–246.

84. Chichilnisky EJ, Kalmar RS. Functional asymmetries in ON and OFF ganglion cells of primate retina. J Neurosci. 2002;22:2737–2747.

85. Fiscella M, Farrow K, Jones IL, et al. Recording from defined populations of retinal ganglion cells using a high-density CMOS-integrated microelectrode array with real-time switchable electrode selection. J Neurosci Methods. 2012;211:103–113.

86. Etienne-Manneville S, Hall A. Rho GTPases in cell biology. Nature. 2002;420:629–635.

87. Fukata Y, Amano M, Kaibuchi K. Rho-Rho-kinase pathway in smooth muscle contraction and cytoskeletal reorganization of non-muscle cells. Trends Pharmacol Sci. 2001;22:32–39.

88. Wettschureck N, Offermanns S. Rho/Rho-kinase mediated signaling in physiology and pathophysiology. J Mol Med (Berl). 2002;80:629–638.

89. Wiederholt M, Thieme H, Stumpff F. The regulation of trabecular meshwork and ciliary muscle contractility. Prog Retin Eye Res. 2000;19:271–295.

90. Tian B, Gabelt BT, Geiger B, et al. The role of the actomyosin system in regulating trabecular fluid outflow. Exp Eye Res. 2009;88:713–717.

91. Honjo M, Tanihara H, Inatani M, et al. Effects of rho-associated protein kinase inhibitor Y-27632 on intraocular pressure and outflow facility. Invest Ophthalmol Vis Sci. 2001;42:137–144.

92. Epstein DL, Rowlette LL, Roberts BC. Acto-myosin drug effects and aqueous outflow function. Invest Ophthalmol Vis Sci. 1999;40:74–81.

93. Somlyo AP, Somlyo AV. Ca2+ sensitivity of smooth muscle and nonmuscle myosin II: modulated by G proteins, kinases, and myosin phosphatase. Physiol Rev. 2003;83:1325–1358.

94. Nishio M, Fukunaga T, Sugimoto M, et al. The effect of the H-1152P, a potent Rho-associated coiled coil-formed protein kinase inhibitor, in rabbit normal and ocular hypertensive eyes. Curr Eye Res. 2009;34:282–286.

95. Nakajima E, Nakajima T, Minagawa Y, et al. Contribution of ROCK in contraction of trabecular meshwork: proposed mechanism for regulating aqueous outflow in monkey and human eyes. J Pharm Sci. 2005;94:701–708.

96. Bertrand J, Winton MJ, Rodriguez-Hernandez N, et al. Application of Rho antagonist to neuronal cell bodies promotes neurite growth in compartmented cultures and regeneration of retinal ganglion cell axons in the optic nerve of adult rats. J Neurosci. 2005;25:1113–1121.

97. Hu Y, Cui Q, Harvey AR. Interactive effects of C3, cyclic AMP and ciliary neurotrophic factor on adult retinal ganglion cell survival and axonal regeneration. Mol Cell Neurosci. 2007;34:88–98.

98. Sagawa H, Terasaki H, Nakamura M, et al. A novel ROCK inhibitor, Y-39983, promotes regeneration of crushed axons of retinal ganglion cells into the optic nerve of adult cats. Exp Neurol. 2007;205:230–240.

99. Wang M, Zheng Y. Oxidative stress and antioxidants in the trabecular meshwork. PeerJ. 2019;7:e8121.

100. Ammar DA, Hamweyah KM, Kahook MY. Antioxidants protect trabecular meshwork cells from hydrogen peroxide-induced cell death. Translational Vision Science & Technology. 2012;1:4.

101. Böhm EW, Buonfiglio F, Voigt AM, et al. Oxidative stress in the eye and its role in the pathophysiology of ocular diseases. Redox Biology. 2023;68:102967.

102. Majsterek I, Malinowska K, Stanczyk M, et al. Evaluation of oxidative stress markers in pathogenesis of primary open-angle glaucoma. Exp Mol Pathol. 2011;90:231–237.

103. Reis LM, Seese S, Maheshwari M, et al. Novel Genetic Diagnoses in Septo-Optic Dysplasia. Genes (Basel). 2022;13:1165. doi: 10.3390/genes13071165.

104. Wu JI, Rajendra R, Barsi JC, et al. Targeted disruption of Mib2 causes exencephaly with a variable penetrance. Genesis. 2007;45:722–727.

105. Jaglin XH, Poirier K, Saillour Y, et al. Mutations in the beta-tubulin gene TUBB2B result in asymmetrical polymicrogyria. Nat Genet. 2009;41:746–752.

106. Cederquist GY, Luchniak A, Tischfield MA, et al. An inherited TUBB2B mutation alters a kinesin-binding site and causes polymicrogyria, CFEOM and axon dysinnervation. Hum Mol Genet. 2012;21:5484–5499.

107. Ugalde-Triviño L, Tejeda GS, Esteban-Ortega GM, et al. A brain-accessible peptide modulates stroke inflammatory response and neurotoxicity by targeting BDNF-receptor TrkB-T1 specific interactome. Theranostics. 2025;15:4654–4672.

108. Zhang M, Deng Y, Luo Y, et al. Control of BACE1 degradation and APP processing by ubiquitin carboxyl-terminal hydrolase L1. J Neurochem. 2012;120:1129–1138.

109. Bilguvar K, Tyagi NK, Ozkara C, et al. Recessive loss of function of the neuronal ubiquitin hydrolase UCHL1 leads to early-onset progressive neurodegeneration. Proc Natl Acad Sci U S A. 2013;110:3489–3494.

110. Mehalow AK, Kameya S, Smith RS, et al. CRB1 is essential for external limiting membrane integrity and photoreceptor morphogenesis in the mammalian retina. Hum Mol Genet. 2003;12:2179–2189.

111. Weleber RG. Infantile and childhood retinal blindness: a molecular perspective (The Franceschetti Lecture). Ophthalmic Genet. 2002;23:71–97.

112. Massey-Harroche D, Delgrossi M, Lane-Guermonprez L, et al. Evidence for a molecular link between the tuberous sclerosis complex and the Crumbs complex. Hum Mol Genet. 2007;16:529–536.

113. Kukekova AV, Nelson J, Kuchtey RW, et al. Linkage mapping of canine rod cone dysplasia type 2 (rcd2) to CFA7, the canine orthologue of human 1q32. Invest Ophthalmol Vis Sci. 2006;47:1210–1215.

114. van de Pavert SA, Meuleman J, Malysheva A, et al. A single amino acid substitution (Cys249Trp) in Crb1 causes retinal degeneration and deregulates expression of pituitary tumor transforming gene Pttg1. J Neurosci. 2007;27:564–573.

115. Di Donato N, Neuhann T, Kahlert A, et al. Mutations in EXOSC2 are associated with a novel syndrome characterised by retinitis pigmentosa, progressive hearing loss, premature ageing, short stature, mild intellectual disability and distinctive gestalt. J Med Genet. 2016;53:419–425.

116. Weatherly SM, Collin GB, Charette JR, et al. Identification of Arhgef12 and Prkci as genetic modifiers of retinal dysplasia in the Crb1rd8 mouse model. PLoS Genet. 2022;18:e1009798.

117. Manavathi B, Peng S, Rayala SK, et al. Repression of Six3 by a corepressor regulates rhodopsin expression. Proc Natl Acad Sci U S A. 2007;104:13128–13133.

118. Bock C, Datlinger P, Chardon F, et al. High-content CRISPR screening. Nature Reviews Methods Primers. 2022;2:8.

119. Duong TT, Vasireddy V, Ramachandran P, et al. Use of induced pluripotent stem cell models to probe the pathogenesis of Choroideremia and to develop a potential treatment. Stem cell research. 2018;27:140–150.

120. Sullivan SK, Mills JA, Koukouritaki SB, et al. High-level transgene expression in induced pluripotent stem cell–derived megakaryocytes: correction of Glanzmann thrombasthenia. Blood. 2014;123:753–757.

121. Maguire JA, Gagne A, Mills JA, et al. Generation of human control iPS cell line CHOPWT9 from healthy adult peripheral blood mononuclear cells. Stem Cell Research. 2016;16:14–16.

122. Espuny-Camacho I, Michelsen KA, Gall D, et al. Pyramidal neurons derived from human pluripotent stem cells integrate efficiently into mouse brain circuits in vivo. Neuron. 2013;77:440–456.

123. Borghuis BG, Tian L, Xu Y, et al. Imaging light responses of targeted neuron populations in the rodent retina. J Neurosci. 2011;31:2855–2867.

Figure 1: Constructing cRE network of glaucoma relevant eye cell types using a trifecta of genomic assays

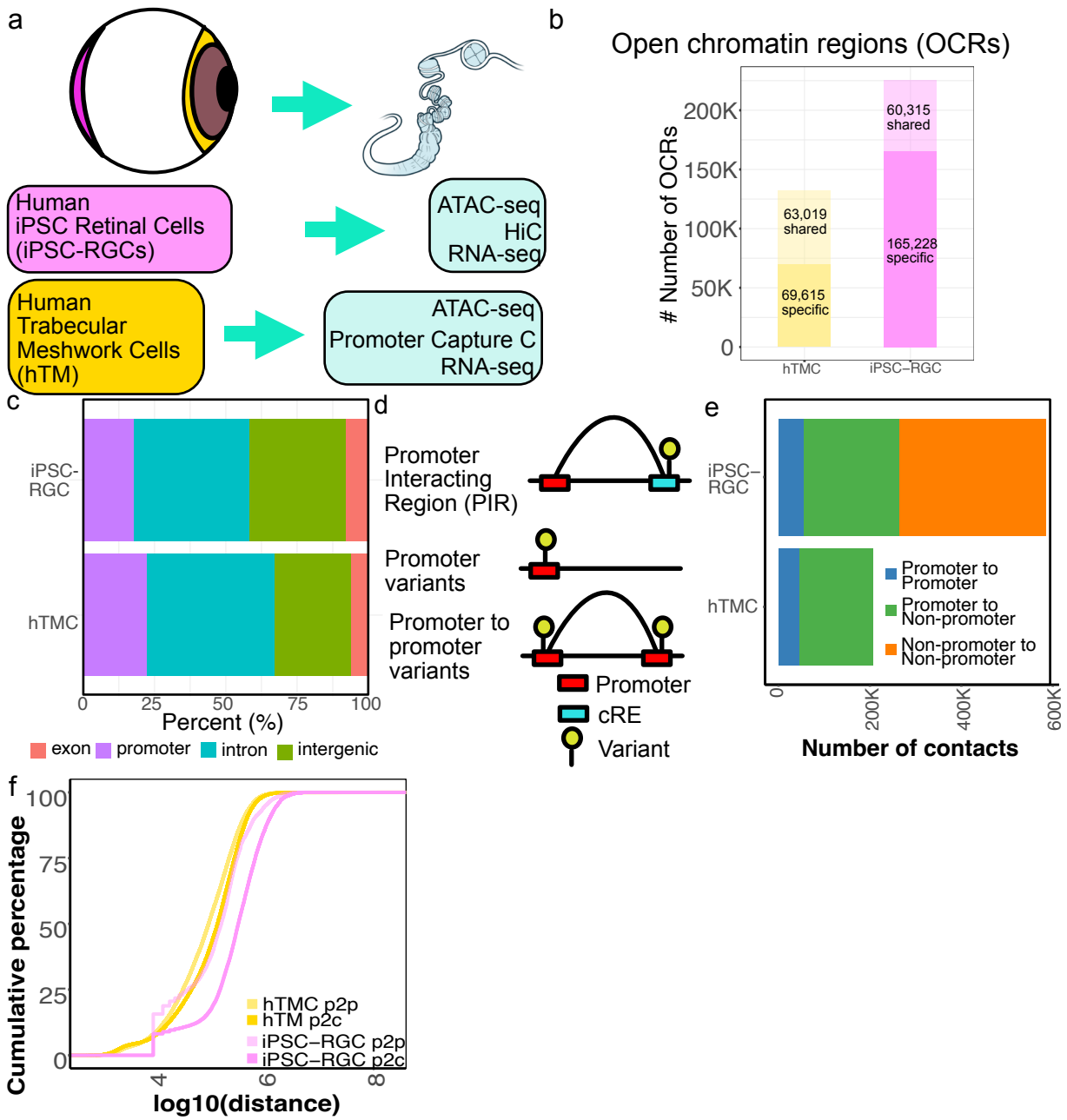

Figure 2: Promoter connected OCRs are correlated with increased expression

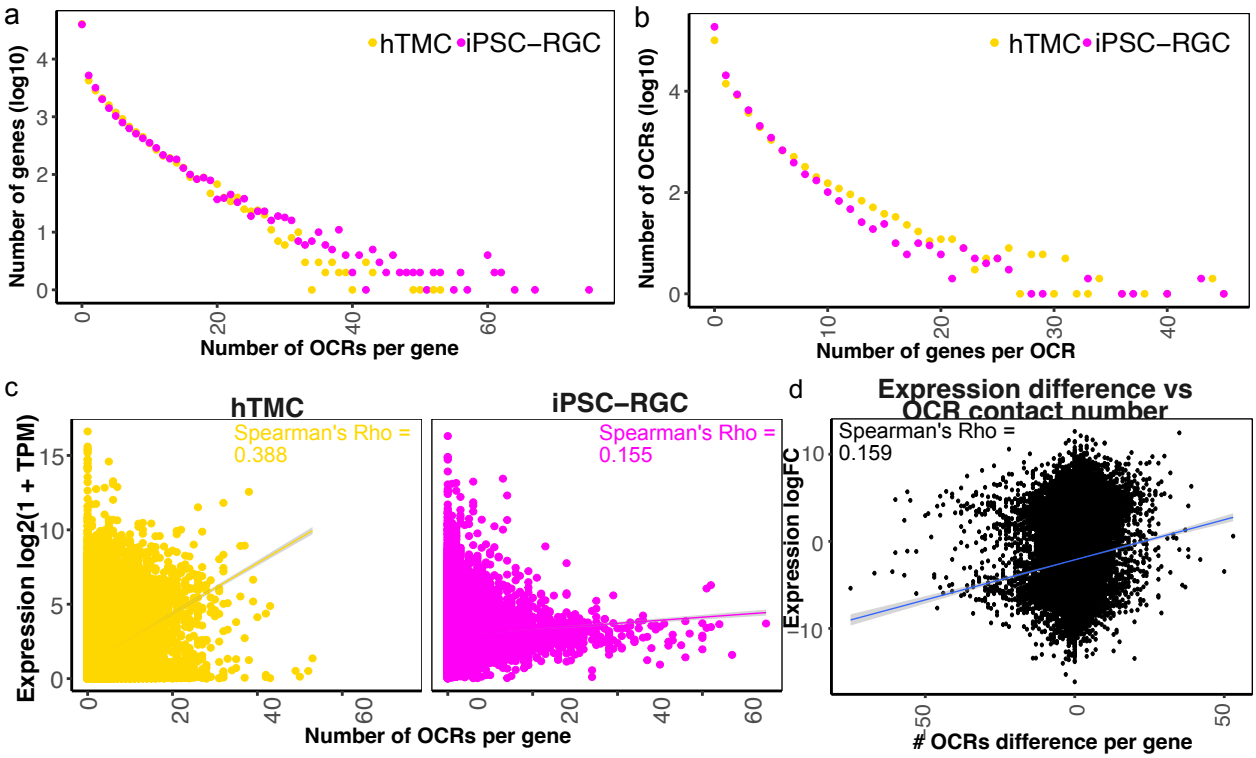

Figure 3: Cell type enrichment results for eye-relevant traits

Figure 4: Quantitative mRNA expression analyses of prioritized genes implicated in hTMCs and hiPSC-RGCs

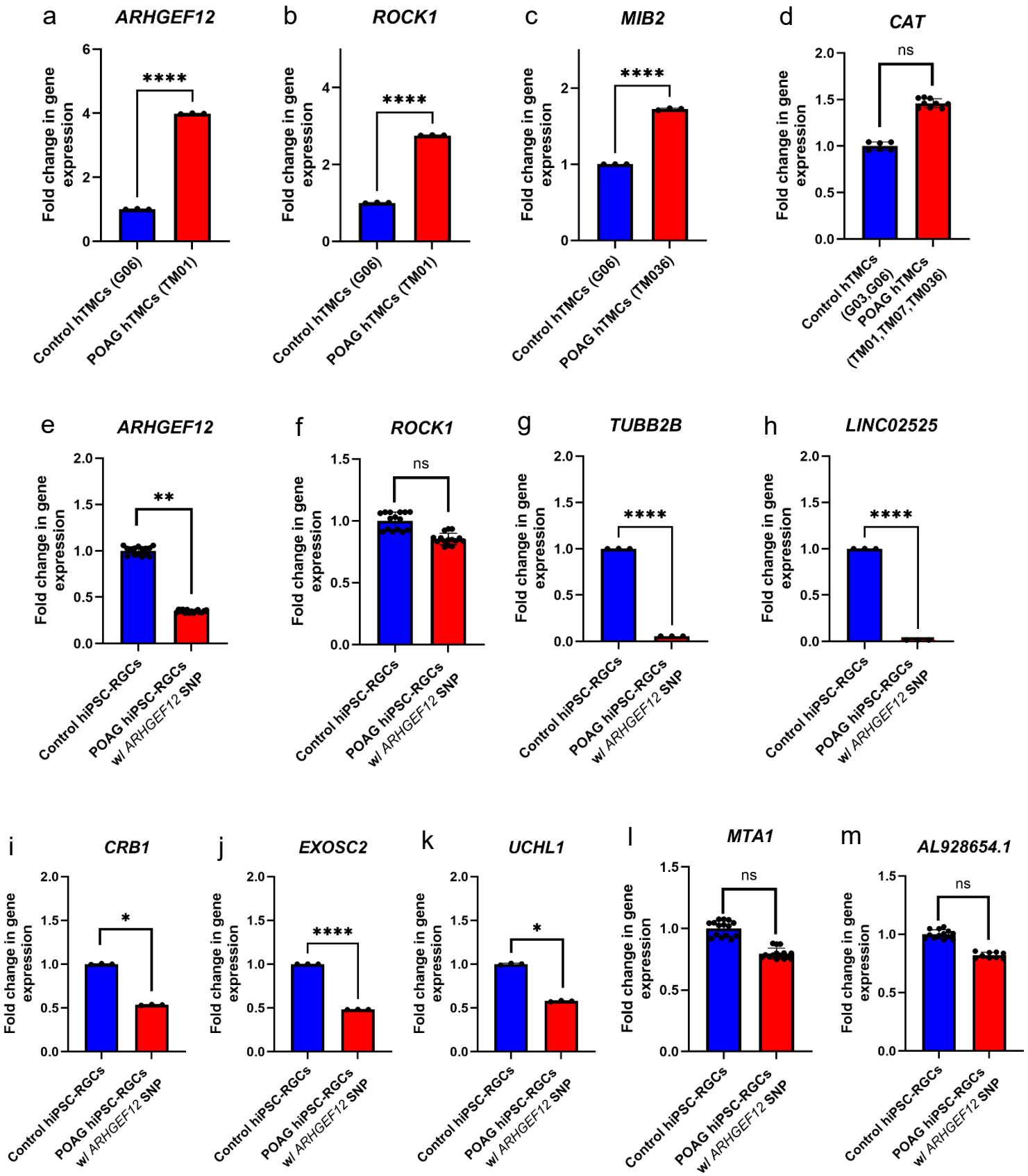
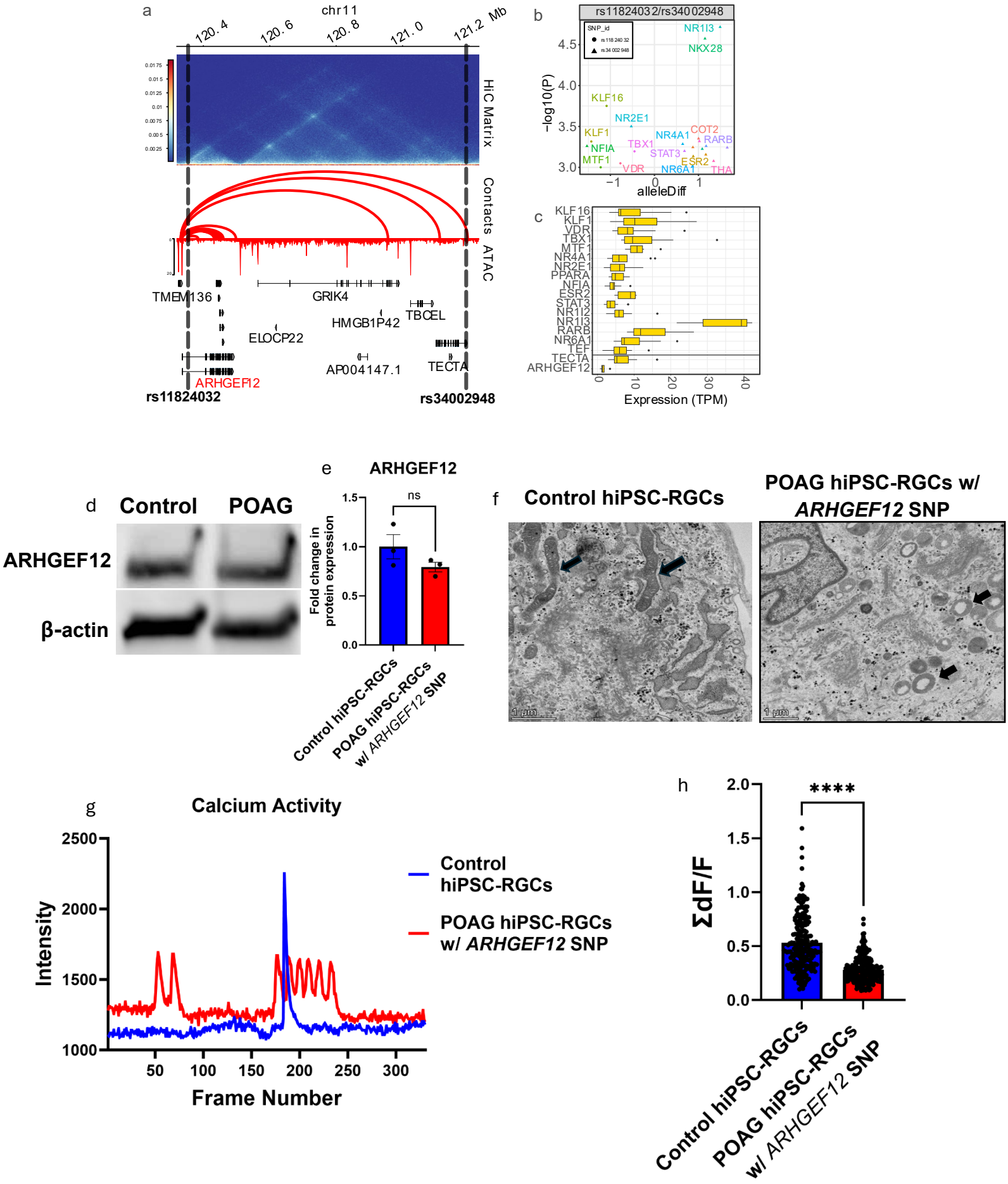
Figure 5: Nomination of *ARHGEF12* as a putative effector gene for POAG AFR ancestry GWAS variant in hiPSC-RGCs